Influence of constituent particles on fracture of aluminum alloys under high-triaxiality loading

Lars Edvard Blystad Dæhli [a,b,*], Sindre Nordmark Olufsen [a,b], Tore Andre Kristensen [c], Tore Børvik [a,b], Odd Sture Hopperstad [a,b]

[a] *Structural Impact Laboratory (SIMLab), Department of Structural Engineering, NTNU – Norwegian University of Science and Technology, Richard Birkelands vei 1A, 7034 Trondheim, Norway*
[b] *Centre for Advanced Structural Analysis (CASA), Department of Structural Engineering, NTNU – Norwegian University of Science and Technology, Richard Birkelands vei 1A, 7034 Trondheim, Norway*
[c] *Sintef Industry, Materials and Nanotechnology, Richard Birkelands vei 1C, 7034 Trondheim, Norway*

ARTICLE INFO

ABSTRACT

Single-edge notch bending tests are conducted to study the influence of constituent particles on the fracture resistance of aluminum alloys 6061, 6063, and 6110 under high-constraint loading conditions. The alloys are tested in the as-cast state after homogenization and artificial aging to temper T6. Each alloy type was delivered with two different volume fractions of constituent particles to enable a quantitative assessment of its impact on the toughness of these aluminum alloys. One variant corresponds to the commercial alloy, whereas the other variant is tailor made with an increased amount of constituent particles by adding Fe and Si to the commercial alloy. All alloys exhibit a dendritic structure with particles clustered at grain boundaries and dendrite arm boundaries. The increased content of constituent particles in the tailor-made alloys is shown to be purely detrimental for the toughness and reduces relevant fracture energy parameters by more than 50% in the alloys tested herein. In the plane-strain-dominated regions of the specimens where the stress triaxiality is highest, crack propagation was found to take place on grain boundaries and dendrite arm boundaries due to void nucleation, growth, and coalescence from the constituent particles. Differences in toughness between the alloys are primarily related to variations in the content, size, and spacing of the constituent particles. A comparison between the three different alloy types, i.e. 6061, 6063, and 6110, shows that strength affects the toughness, but it does not follow the commonly reported trade-off between strength and ductility.

1. Introduction

Ductile fracture in structural alloys can take place by several mechanisms [1], but is commonly associated with void nucleation, growth, and coalescence [2,3]. Microscopic voids have been found to pre-exist in the material [4,5], but are usually considered to nucleate from particles by cracking or particle–matrix decohesion [2,3,6–9]. Particle content, size, and spatial distribution are therefore considered key parameters for the ductility and toughness properties of structural alloys, as shown for instance in the work of Hannard et al. [10].

Aluminum alloys are widely used for structural applications as they offer high strength-to-weight ratios, good formability and corrosion resistance, and have an excellent potential for recycling. Commercial, heat-treatable aluminum alloys contain second-phase particles of various composition, size and shape. These are broadly categorized as precipitates, dispersoids, and constituent particles and their sizes are

typically on the ranges of 0.005–0.1 μm, 0.1–1 μm, and 0.5–50 μm, respectively [6,11–14]. The constituent particles are formed during casting and are usually Fe-rich, since iron is very difficult to remove from the molten metal and has low solubility in aluminum [15–17]. The constituent particles are insoluble, but may transform into other phases. In the 6000-series aluminum alloys, the particles formed during casting are mainly Mg_2Si and brittle, plate-like β-AlFeSi, which are known to lower the workability and ductility of the alloy, and cause poor surface finish of extruded components [18–22]. A subsequent homogenization treatment dissolves Si eutectics and low-melting Mg_2Si, which may precipitate in the form of smaller β'-Mg_2Si particles upon cooling [23], and transforms the β-AlFeSi particles into more rounded α-AlFeSi particles. These constituent particles remain as hard inclusions in the alloy [19]. The composition of the constituent particles varies depending on the excess alloying elements (e.g. Mg and Si) and transition elements (e.g. Mn

and Cr) of the alloy [15,17,24,25], but in the DC-cast 6061, 6063, and 6110 aluminum alloys tested by Thomesen et al. [26] the particles mainly had a composition close to $Al_{50}(Fe,Mn,Cr)_{12}Si_7$. The dispersoids are usually formed during homogenization. These are typically rich in transition elements (e.g. Mn or Cr) and distributed rather homogeneously in the grain interior. The strengthening precipitates are formed from atomic clusters during artificial aging and transform through a sequence of different precipitation phases [27]. Peak strength condition (temper T6) is achieved by a combination of coherent GP-zones and semi-coherent, needle-shaped β'' precipitates [28,29].

All three groups of particles influence the mechanical properties of the alloy in various ways and to various extent. Assessing the influence of the different particle types is quite challenging, since there is generally a complex interplay between all particles. Microstructural alterations that are imposed to vary certain characteristics of one particle type would normally also influence other particle types, making it more difficult to study the influence of each particle type separately. Multiscale models developed to account for effects of precipitates, dispersoids, and constituent particles have revealed that ductility and toughness are governed by a trade-off in the relative content of various particles, and that the interplay between different particles is affected by the matrix strength and hardening properties [14,30].

Precipitates are mainly favorable for the alloy's properties. They are effective obstacles for dislocations and thereby increase the strength of the alloy. However, void nucleation occurs more readily at higher stress levels, so that the precipitates may also inflict a negative effect on the ductility and toughness [12,13,30–32]. Ductility and toughness have been found to decrease up to peak aging, which is the state where the precipitates have the largest contribution to strength, and then increase again in the overaged state [13,33]. Increasing the strength and lowering the hardening capacity generally tend to reduce material ductility and toughness [6,13,32–36].

The influence of the dispersoids on ductile fracture depends on competing mechanisms [37] and somewhat conflicting observations are reported in the literature. A higher dispersoid content has been found to enhance ductility and toughness in some studies, where the positive effect is usually attributed to a more homogeneous distribution of plastic slip and a transition from intergranular to transgranular failure [11,38–40]. On the contrary, dispersoids have also been shown to nucleate secondary voids that expedite the coalescence process and truncate primary void growth by void-sheeting [6,41–44]. Bron et al. [45] observed that dispersoids nucleated secondary voids within localization bands in the slant fracture regions of their test specimens. Also, Liu et al. [14] tested two different aluminum alloys with varying dispersoid content, induced by different homogenization treatments and artificial aging, and their results show that dispersoids can significantly influence ductility and toughness depending upon their size and spacing. Numerical finite element simulations [46–49] have also shown that a secondary void population between the larger, primary voids expedites void coalescence, but that it is less important in the void growth stage. Similar results have been reported from experiments, for instance by Garrett and Knott [34] who observed that void nucleation from dispersoids occurred only after onset of localized plastic deformations. The dispersoids were thus found to mainly affect the strength and hardening capacity of the matrix, while the influence on fracture toughness was minor.

Although both precipitates and dispersoids may constitute a significant contribution to the ductile fracture process, the constituent particles are usually considered to be most detrimental for the ductility and toughness (see e.g. Hahn and Rosenfield [6], Blind and Martin [11] and Van Stone et al. [44]). The constituent particles are quite large and easily bypassed by dislocations, thus offering little contribution to the yield strength and work hardening [23,32], but are expected to have a higher propensity for void nucleation [2,10,22,34,42,44,50] and lead to higher void growth rates [42,44] than smaller particles. Shen et al. [51] and Petit et al. [52] for instance observed that damage initiated from

large Mg_2Si particles, and later at large iron-rich intermetallic particles, in a 6061 aluminum alloy. Also, Liu et al. [13] have found that the ductility was reduced by more than 50% when the constituent-particle content was only 1%, as compared to a constituent-particle-free material, based on multi-scale model simulations. Hence, the constituent particles have a deleterious effect on the ductility and toughness of the alloy and the amount of constituent particles should be kept as low as possible. It is well known that the fracture properties of an alloy can be enhanced by producing cleaner alloys, such as reducing the content of particle-forming elements (e.g. Fe and Si), or by optimizing the manufacturing process (e.g. altering the solution treatment) such that the formation of the most detrimental particles is avoided [30,44]. However, removing impurities such as iron from the molten aluminum metal is very costly, and therefore not economically feasible for commercial alloys, while production processes have been subject to enhancements for many years and are already quite optimized. Constituent particles are therefore normally always present. Another aspect of emerging relevance is the increasing use of recycled aluminum to meet the emission reduction goals [53]. The recycling process is inherently associated with contamination and accumulation of impurity elements that can significantly elevate the content of constituent particles [54,55] and thereby alter the ductility and toughness of these alloys. This serves as a motivating factor for the current study.

The detrimental effect of constituent particles on ductility and toughness is firmly established in the literature, but is largely based on test data deriving either from different alloys or from alloys subjected to different heat treatments. To study the influence of constituent particles alone, it is however necessary to test alloys where other microstructural properties (e.g. grain size, precipitate structure, dispersoid content, etc.), and thereby strength and work-hardening capacity, are largely unaltered. Bron et al. [45] performed various mechanical tests on one commercial and one high-purity variant of the AA2024 alloy, in which the commercial alloy had about three times higher particle content. While the two alloys had similar tensile properties, it was found a notable improvement of the damage resistance in the high-purity alloy. Das et al. [56] examined the effect of elevated Fe-content on the formability of aluminum alloys 6022 and 5182, and found that the formability was significantly reduced when the Fe-content was elevated. The influence of increased constituent particle content on tensile ductility and tearing resistance of various 6000-series aluminum alloys in the as-cast and homogenized state was recently studied by Tomstad et al. [57] and Qvale et al. [58]. Similarly, the effects of constituent particles on tensile ductility and shear ductility of extruded 6000-series aluminum alloys were respectively examined by Tomstad et al. [57,59]. In their alloys, the constituent-particle content was increased by adding balanced amounts of Si and Fe in a commercial alloy type, which enabled to vary the particle content while retaining the grain structure, strength, and work-hardening capacity. As a general result, all these three studies found a pronounced, detrimental effect of the constituent particles on the alloys' damage resistance. In some cases the alloy experienced a reduction in the damage resistance of more than 50% when the constituent particle content was increased by a factor of around three [57,58]. It should be noted that the negative effect of the constituent particles was found to be much greater for as-cast and homogenized alloys than for extruded alloys, which was attributed to a re-distribution of the void-nucleating particles to the grain interior during extrusion [57].

The current study examines the role played by the constituent particles in limiting the toughness of three different aluminum alloys. It extends the previous work of Tomstad et al. [57] and Qvale et al. [58], which was focused on tensile ductility and tearing resistance, to include loading conditions governed by very high stress triaxiality ratios. Single-edge notch bending (SE(B)) tests are performed on two variants of 6061, 6063, and 6110 aluminum alloys in the as-cast state after homogenization and artificial aging to temper T6: the first variant corresponds to the commercial alloy type, whereas the second variant

Table 1

Chemical composition of the six aluminum alloys in wt-%.

Alloy	Mg	Si	Fe	Cu	Mn	Zn	Ti	Cr	Al
6061A	0.903	0.621	0.209	0.204	0.038	0.054	0.106	0.060	Bal.
6061B	1.017	0.811	0.766	0.189	0.040	0.053	0.116	0.071	Bal.
6063A	0.470	0.512	0.206	0.001	0.047	0.003	0.006	0.001	Bal.
6063B	0.481	0.692	0.753	0.001	0.048	0.004	0.015	0.005	Bal.
6110A	0.828	0.720	0.196	0.203	0.506	0.003	0.026	0.157	Bal.
6110B	0.793	0.925	0.749	0.204	0.503	0.005	0.029	0.183	Bal.

corresponds to a tailor-made type with an elevated content of iron-rich constituent particles. Results from the SE(B) tests corroborate the results and conclusions of the previous studies by Tomstad et al. [57], Qvale et al. [58] and Tomstad et al. [59], and clearly demonstrate that the constituent particles have a primary influence on the toughness of the alloys considered in this study.

2. Materials

2.1. Overview of alloys

Aluminum alloys 6061, 6063, and 6110 are used in the SE(B) tests conducted in this work. Each alloy was provided in two different configurations governed by the constituent-particle content. The commercial alloys have the lowest content of constituent particles. These were characterized and tested by Thomesen et al. [26]. An additional set of alloys was tailor-made with a higher content of constituent particles by adding Fe and Si to the commercial alloys. The amount of added Si was adjusted to retain the same level of Si in solid solution in the tailor-made alloys as in the commercial alloys. Otherwise, the strength and work-hardening properties would differ between the two alloy variants, which have an influence on the ductility and fracture characteristics [17,23]. The chemical composition of the alloys is listed in Table 1.

All alloys were received as DC-cast extrusion billets with a diameter of 95 mm and were delivered by Hydro R&D Sunndal. The billets were homogenized according to industrial practice before delivery. To keep consistent with the notation used in previous studies on the same alloys [57–59], the three commercial alloys with low constituent-particle content are referred to as A-alloys or A-variants, whereas the tailor-made alloys with higher constituent-particle content are referred to as B-alloys or B-variants.

Material pieces with a size of 11 mm × 11 mm × 70 mm were cut out from the extrusion billets. The material pieces were extracted approximately 30 mm from the center of the billets to avoid sampling artefacts and material defects from regions close to the billet surface. All material pieces were then solution heat-treated and artificially aged to temper T6 by the following procedure [26]:

- Solution heat treatment at 560 °C for 10 min, followed by water-quenching.
- Storage at room temperature for 24 h.
- Artificial aging at 180 °C for 8 h, followed by water-quenching.

2.2. Initial microstructure

The initial material microstructure of the A-alloys and the B-alloys was characterized in the work of Thomesen et al. [26] and Tomstad et al. [57], respectively. Therein, grain structure images were acquired by optical microscopy, whereas the particle distributions were characterized from backscatter electron micrographs obtained with a scanning electron microscope (SEM). Different types of constituent particles form during solidification and homogenization. The majority of the constituent particles is assumed to be variants of α-AlFeSi [16,19]. Thomesen et al. [26] characterized the chemical composition of many constituent particles in the A-alloys using energy dispersive spectroscopy (EDS) and found that they mainly had a composition

Table 2

Microstructure data of the six aluminum alloys. Average grain size (D_g), area fraction of particles (f_p), mean particle size (D_p), minimum ($D_{F,min}$) and maximum ($D_{F,max}$) Feret diameters are given in the table. Particle size and Feret diameters for each alloy are given in terms of the mean value and the standard deviation ($\mu_N \pm \sigma_N$) calculated from the measurement data. The number of particles per square millimeter (N_p/mm^2) from the particle analysis is given in the last column. Note that these data are rendered from data published in previous studies on the same alloys [26,57,58].

Alloy	D_g [μm]	f_p [–]	D_p [μm]	$D_{F,min}$ [μm]	$D_{F,max}$ [μm]	N_p/mm^2
6061A	124.0	0.0050	0.59 ± 0.37	0.46 ± 0.28	0.92 ± 0.82	13 087
6061B	101.4	0.0172	0.79 ± 0.49	0.62 ± 0.40	1.36 ± 1.14	25 405
6063A	63.2	0.0061	0.94 ± 0.55	0.67 ± 0.42	1.67 ± 1.45	6616
6063B	58.3	0.0199	0.96 ± 0.56	0.74 ± 0.47	1.69 ± 1.52	20 417
6110A	66.7	0.0077	1.01 ± 0.67	0.78 ± 0.55	1.76 ± 1.60	6616
6110B	72.4	0.0240	0.92 ± 0.54	0.75 ± 0.53	1.63 ± 1.35	26 660

close to $Al_{50}(Fe,Mn,Cr)_{12}Si_7$. We assume herein that the same type of particles will form in the B-alloys.

All alloys have a dendritic grain structure with nearly equiaxed grains, as shown in Fig. 1, which is typical for cast alloys [23,32]. Grain orientations have not been measured in this work, but since the alloys are in the as-cast state they are assumed to have a random texture and thus exhibit nearly isotropic behavior, which has been verified for various aluminum alloys in previous studies (e.g. [32]). The 6061 alloys have the largest average grain size, with some grains more than 200 μm in size, whereas the 6063 and 6110 alloys comprise smaller grains. The A- and B-variants of a certain alloy have comparable grain size, as inferred from the average grain size (D_g) listed in Table 2, and the largest difference is found between 6061A and 6061B. We thus conclude that the grain structure is largely unaffected by the addition of Fe and Si in the B-alloys.

The grain images in Fig. 1 show that the constituent particles mainly reside at the grain boundaries and the dendrite arm boundaries (inter-dendritic regions) within the grains. Visual inspection readily confirms that the amount of constituent particles is much higher in the B-alloys than in the A-alloys. The constituent-particle content (f_p), particle size (D_p), minimum and maximum Feret diameters ($D_{F,min}$, $D_{F,max}$), and number of particles per square millimeter (N_p/mm^2) determined from several SEM images for each alloy are listed in Table 2. Particles smaller than 0.2 μm were excluded in the particle analysis as they are assumed to be dispersoids [26,57]. The particle size and Feret diameters are given in terms of their mean value (μ_N) and standard deviation (σ_N). The particle size is defined as the diameter of a circle having the same area as the measured particle, i.e. $D_p = \sqrt{4A_{meas}/\pi}$ [17,57]. Note that the values of the particle size and Feret diameters listed in this table deviate from those reported by Tomstad et al. [57] and Qvale et al. [58] since those authors used area-averaged values, while here we use arithmetic mean values. The SEM images presented in Thomesen et al. [26] and Tomstad et al. [57] showed that all six alloys contain elongated particles, and the minimum and maximum Feret diameters listed in Table 2 yield aspect ratios in the range $D_{F,min}/D_{F,max} \in [0.518, 0.592]$. However, as noted by Tomstad et al. [57], the particles have random orientation and are assumed to exhibit isotropic properties on average. The particle content (f_p) is about three times higher in the B-alloys than in the A-alloys due to the added Fe and Si. Correspondingly, the particle density (number of particles per square millimeter) is much higher in the B-alloys. Note that the particle density in 6061A is substantially higher than in 6063A and 6110A, despite the lower particle volume fraction in the former. This is due to the lower particle size in 6061A, which is only about half compared to the 6063 and 6110 alloys.

Particle size distributions (PSDs) of the alloys are plotted in Fig. 2. Each histogram has a bin size of 0.1 μm and is plotted in terms of the probability density calculated from the particle size measurements. In all the figures, blue histograms correspond to data for the A-alloys and orange histograms correspond to the B-alloys. The expression for a log-normal probability density function (PDF) of the particle size
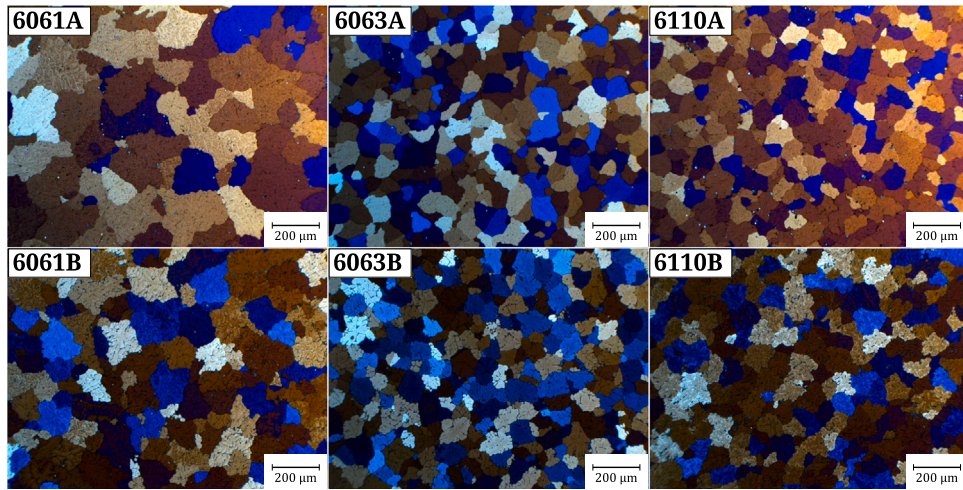
Fig. 1. Initial grain structure of the alloys. Primary particles are visible at grain boundaries and dendrite arm boundaries.
Source: The grain structure images were acquired by Thomesen et al. [26] and Tomstad et al. [57].
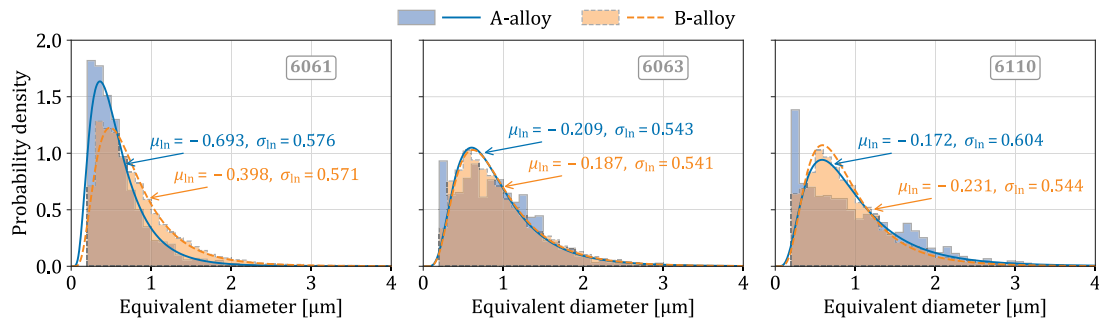

Fig. 2. Particle size distributions in terms of equivalent diameter for the six alloys: (A) 6061, (B) 6063, (C) 6110. The *y*-axis corresponds to the probability density function.

distribution is plotted on top of each histogram. The log-normal PDF of the particle size D_p is given by

$$f(D_p) = \frac{1}{D_p \sigma_{ln} \sqrt{2\pi}} \exp\left(-\frac{(\ln D_p - \mu_{ln})^2}{2\sigma_{ln}^2}\right) \qquad (1)$$

where the log-normal mean and standard deviation, denoted μ_{ln} and σ_{ln}, are calculated from the mean and standard deviation of the particle measurements (μ_N, σ_N) using

$$\mu_{ln} = \ln\left(\frac{\mu_N}{\sqrt{1 + \sigma_N^2/\mu_N^2}}\right), \;\; \sigma_{ln} = \sqrt{\ln\left(1 + \frac{\sigma_N^2}{\mu_N^2}\right)}. \qquad (2)$$

The results for the A- and B-variants of each alloy are plotted with solid, blue lines and dashed, orange lines, respectively. The parameters governing each of the lognormal PDFs are given in Fig. 2, whereas the associated mean and standard deviations from the particle measurements conducted by Thomesen et al. [26] and Tomstad et al. [57] are listed under D_p in Table 2. Note that PSD plots of these alloys have been presented in earlier studies [26,57,58], but these were given in terms of the area fraction of particles rather than the number fraction.[1]

Fig. 2 shows that most of the constituent particles are quite small, with an equivalent circle diameter below 1 μm, in all six alloys. While

the mean particle size is similar in 6063A and 6063B, the A- and B-variants of the 6061 and 6110 alloys have different mean particle sizes (see Table 2). In the case of 6061, the particles are larger in the B-variant than in the A-variant, while for 6110 the particles are larger in the A-variant than in the B-variant. This is reflected by the PSDs shown in Fig. 2, where we infer that 6061B is shifted towards larger particles compared to 6061A, while the opposite is observed for the 6110 alloys. Although 6063A and 6063B have similar mean and standard deviation of the particle size, it seems that the PSD for 6063A exhibits somewhat more dispersion around the mean value. A similar observations is made for 6110A. It is noted that fewer particles are included in the particle analyses of the A-alloys, both due to the particle density and the area used in the characterization [57], and 6063A and 6110A had the lowest number of particles ($N_p \approx 1500$) included in the particle analysis, which might explain the larger degree of dispersion observed for these two alloys.

Pair correlation function (PCF) plots [60,61] are presented in Fig. 3. The PCFs were generated by looping through the constituent particles in SEM images sequentially and identifying the position of all neighboring particles within a square window of size 20 μm × 20 μm while the particle under consideration is placed in the center [57]. The PCF plots are interpreted as follows: a high scalar value (i.e. yellow color) indicates a high probability of finding a particle in that region, whereas a low scalar value (i.e. blue color) indicates a correspondingly low probability. If the particles are uniformly distributed, the PCF plots display a uniform color with a unity value.

Fig. 3 shows that the particles in these alloys have a tendency to cluster, but the near radial symmetry of the PCF plots implies that the clusters are randomly distributed in the material. This is in accordance with the observation that the particles reside predominantly
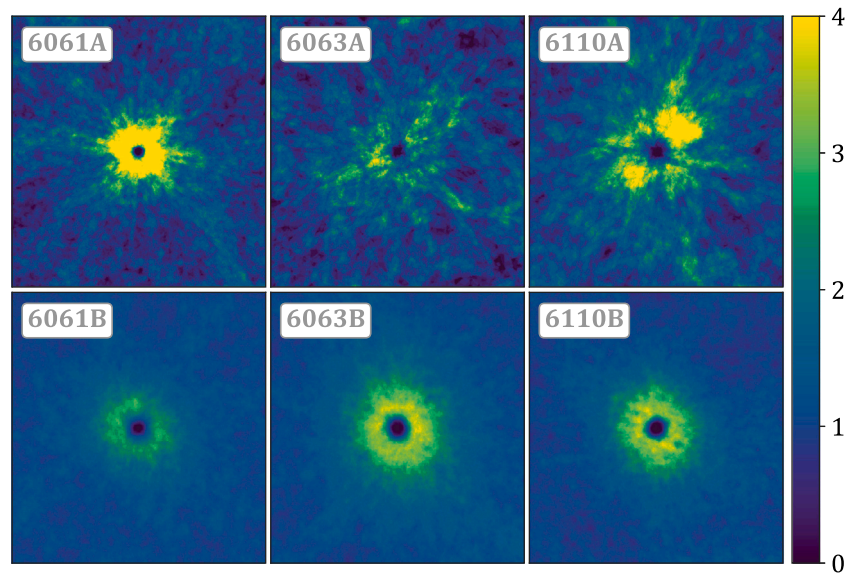
---

[1] The rationale for using the latter herein is that it gives a somewhat different impression of the particle content in these alloys and makes the data more accessible for computational studies where spatial heterogeneity based on the particle content is taken into account.

Fig. 3. Pair correlation function (PCF) plots for the six aluminum alloys computed from a 20 μm × 20 μm square. The PCFs are replotted based on the data of Tomstad et al. [57].

at the grain and dendrite arm boundaries (see Fig. 1). The spatially heterogeneous distribution of the constituent particles leads to a short-range clustering, with a higher probability of finding a particle close to the particle than farther away, but since the grain boundaries and dendrite arms extend randomly in all directions there is no directional preference on average. Note that the radial symmetry is not as apparent for the 6063A and 6110A alloys, which – similar to the dispersion in the PSDs – can be explained from the lower number of particles included in the particle analysis of these alloys.

2.3. Previous mechanical test results

The material behavior of the alloys used in this study have previously been examined through tension tests on axisymmetric smooth and notched samples having a notch radius of $R = 2$ mm and $R = 0.8$ mm by Thomesen et al. [26] and Tomstad et al. [57], and Kahn tear tests by Qvale et al. [58]. Relevant test data from these studies are re-printed here for the sake of completeness and to aid the discussion of the results from the SE(B) tests. The reader should consult the original work for details regarding the experiments. Stress–strain data from the tensile tests and force–notch opening displacement (NOD) data from the Kahn tests are shown in Figs. 4(a) and 4(b), respectively. From left-to-right, the figures correspond to the 6061, 6063, and 6110 alloys.

Key takeaways from the previous mechanical tests are briefly summarized below. The tension tests showed that:

- 6061A and 6110A have comparable strength, while the leaner 6063A has lower strength.
- 6061A and 6063A have comparable ductility, whereas 6110A has much lower ductility.
- 6061A has a superior combination of strength and ductility compared to 6063A and 6110A, which can be attributed both to the lower particle content and the smaller particle size in 6061A [57,58].
- The stress–strain behavior is rather similar between the A-variant and the B-variant of each alloy. However, some minor differences are noted:
  - The B-variants exhibit slightly higher hardening rate for small strains, while the hardening rate of the A-variants is slightly higher at large strains.

  - 6063B has a slightly higher strength than 6063A, which was attributed to a small increase in the content of strengthening precipitates or solute content in 6063B [57].

- The ductility is reduced for the B-variants compared to the A-variants, and the ductility reduction is most pronounced for 6061B and 6110B.
- There is a significant notch sensitivity for all alloys, i.e. a strong influence of stress triaxiality on ductile fracture.

The Kahn tear tests showed that:

- All A-variants exhibit a higher peak force and a higher Notch Opening Displacement (NOD) at peak force than the corresponding B-alloys.
- Generally more scatter for the B-variants, especially in the case of 6061B and 6110B.
- Tearing resistance is reduced for the B-variants, which agrees well with the lower ductility exhibited by these alloys.
- Reduction in tearing resistance for the B-variants is similar between the three alloy types.

3. Experiments

3.1. Three-point bending tests

Three-point bending tests have been performed on SE(B) specimens following the standard BS 7448-1:1991. The specimen geometry and dimensions are shown in Fig. 5(a) and details of the notch region are provided in Fig. 5(c). After artificial aging to temper T6, the material pieces (see Section 2.1) were ground and polished to the final dimensions 10 mm × 10 mm × 70 mm. The machined notch and the grips for the clip gauge in the central part of the specimens were prepared using spark erosion and the specimens were then subjected to fatigue pre-cracking. The fatigue crack extended approximately 1.5 mm from the machined notch towards the specimen center. The initial crack length is thus about $a_0 = 5$ mm, whereas the specimen width is $W = 10$ mm, such that the initial crack length-to-specimen width ratio is approximately $a_0/W = 0.5$. The specimen thickness is $B = 10$ mm. Note that the fatigue crack in reality deviates from the idealistic conditions depicted in Fig. 5(c): the initial crack is not perfectly straight, the crack depth varies slightly through the thickness, and the fatigue crack normally
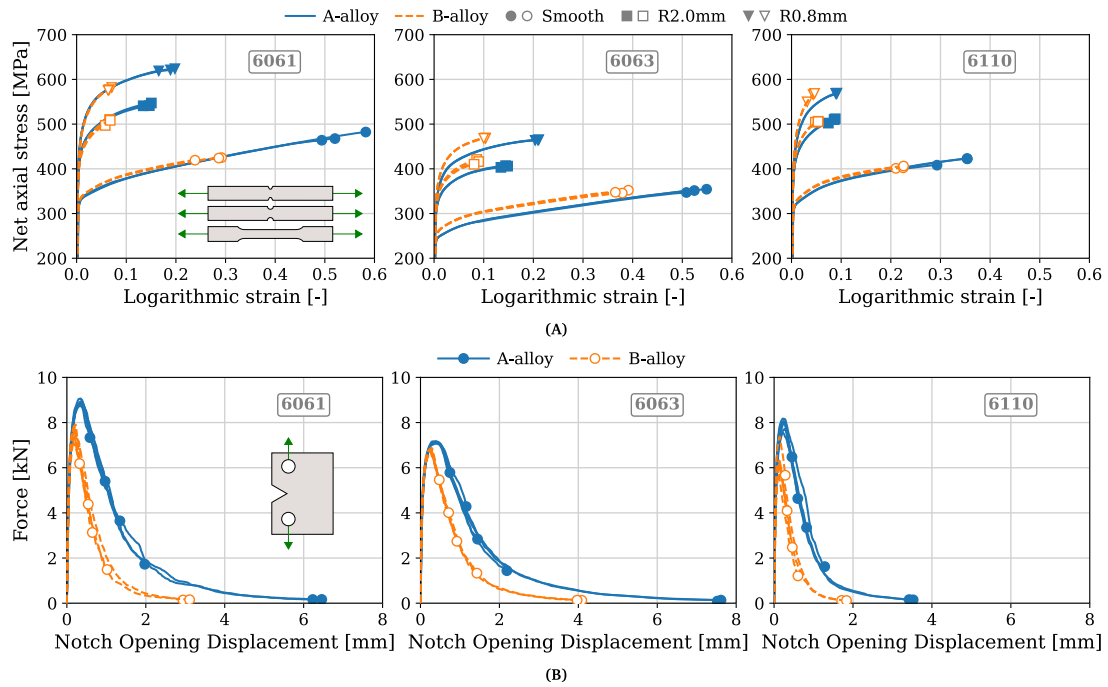
Fig. 4. (A) Stress–strain data from smooth and notch (with notch radius $R = 2$ mm and $R = 0.8$ mm) tension tests [26,57] plotted up to maximum net axial stress and (B) force–NOD data from Kahn tear tests [58]. A marker is plotted at the failure point of each tension test and at the end of each Kahn tear test in (A) and (B). Further details are provided in the corresponding figure legends.
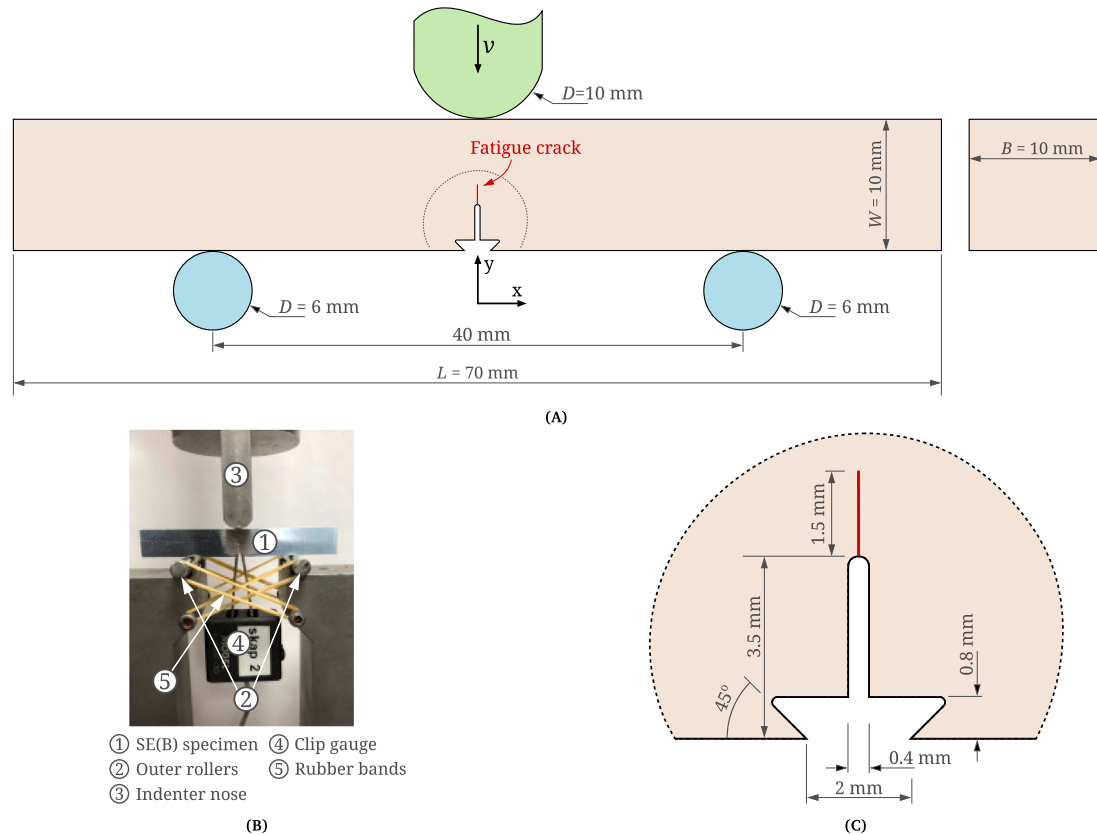

Fig. 5. (A) An illustration of the test setup and relevant dimensions of the SE(B) specimens. (B) A test specimen mounted in the testing machine. The clip gauge used to measure the crack-mouth opening displacement and the rubber bands attached to the supports are shown. (C) A magnified view of the notch region. Note that the fatigue crack in reality deviates from the nominal values indicated in the figure.

initiates off-center from the machined notch root — presumably due to the grain structure.

The test setup is shown in Figs. 5(a) and 5(b). The experiments were performed in a servo-hydraulic Zwick z030 30 kN universal testing machine under displacement control. A rigid indenter with a nose diameter of 10 mm was used to deform the specimens. The specimens were mounted such that the indenter aligned with the center of the pre-machined notch, and were supported by two symmetrically positioned outer rollers with a diameter of 6 mm and a center distance of 40 mm. Rubber bands were attached between the outer rollers and the test rig, as shown in Fig. 5(b), to prevent the supports from moving apart.

The crosshead displacement rate was set to 0.5 mm/min to ensure quasi-static conditions throughout the tests. The force and crosshead displacement were recorded continuously throughout the test. Additionally, a clip gauge was attached between the machined grips at the bottom of the specimen to measure the Crack Mouth Opening Displacement (CMOD) during the test. A Basler acA4112-20um digital camera was used to monitor the specimen surface and the displacement of the indenter nose during the tests. Frictional forces between the specimen and the supports cannot be avoided, but these are considered negligible for the test results. Except for 6061A, three repeat tests were performed on all alloys to large levels of deformation. In the case of 6061A, five tests were performed to different levels of crack propagation to facilitate a study of crack development with increasing external loading.

3.2. X-ray computed tomography

A selection of deformed test specimens were analyzed using X-ray computed tomography (XCT) to reconstruct the crack surface. The XCT setup consists of a Nikon XT H225 ST μCT scanner equipped with a tungsten reflection target and a Perkin Elmer XRD 1620 panel detector with 2000×2000 pixels of 200 μm pixel size and 16-bit pixel depth. Sufficient X-ray transmission was obtained by using an accelerator voltage of 160 kV and a current of 81 μA. The field of view was chosen such that the entire notch region of the specimen was captured, which gives a voxel size of 8.4 μm. During scanning, 3143 radiograms were captured and the tomograms were reconstructed using Nikon CT-Pro 3D.

To facilitate further processing of the tomograms, the noise level was reduced using a 3D-median filter implemented in the image-processing software Fiji [62]. A median filter kernel size of $3 \times 3 \times 3$ voxels was chosen, which reduced the noise level while preserving the topology of the fracture surface. Cross-sectional views of the fracture surfaces were rendered using Fiji, whereas volumetric renderings were produced using Paraview [63].

3.3. Optical microscopy on deformed specimens

In the same specimens analyzed by XCT, the particles and grains in the vicinity of the crack were imaged using a Reichert MeF3A optical microscope. All images were taken on a material section at mid-thickness where we expect the cracks to propagate farthest into the specimens due to crack tunneling. A small volume in the central region of the specimens, including both the notch and the crack ligament, was cut out and sliced in two halves at mid-thickness. The samples were cast in Epofix, ground and polished using various SiC paper and polishing cloths, and then polished with OP-U active oxide suspension for 20 s to obtain a scratch-free surface.

Regular light microscope images were first recorded to visualize the particles and the contours of the crack boundary. The samples were then anodized and reinserted into the light microscope for grain structure imaging using polarized light. These grain structure images of the deformed specimens facilitate a qualitative examination of the governing fracture modes. Both regular light microscope images and grain structure images were taken at various magnifications. Images of the crack surface on the grain structure were finally prepared using an overlay of grain images and regular light microscope images.

4. Results

4.1. Global response

The force vs. crack-mouth opening displacement (CMOD) data recorded from all the tests conducted in this study are shown in Fig. 6. From left-to-right, the graphs in Fig. 6 pertain to test data of 6061 (blue lines with circle markers), 6063 (orange lines with square markers), and 6110 (green lines with triangular markers). Solid lines and filled markers are used for the A-variants (low particle content), whereas dashed lines and open markers are used for the B-variants (high particle content) of each alloy type. The two markers highlight the instance of peak force (first) and the maximum CMOD value (second) obtained during the test, respectively. In the case of 6061A, five tests were performed to different final deformation levels to visualize the crack surface at various load levels using XCT. However, out of the five tests, only four were accepted (and thus shown in Fig. 6) because one of the specimens displayed a much lower initial stiffness due to a problem in the fatigue crack pre-processing of that specimen. Three repeat tests were performed on the five other alloys in which all the specimens were loaded to a highly deformed state. Note that a stiffness-related deviation is also observed in one of the tests on 6110B, but this deviance is much less pronounced and the test was therefore still included in the data set.

Increasing the constituent-particle content clearly has a negative effect on the toughness. The peak force and the CMOD at peak force are both reduced in the B-alloys, but the magnitude of the reduction varies between the alloys. The 6061 alloy exhibit the largest influence of particle content, inferred from the large reduction in both the peak force and the CMOD at peak force in 6061B compared to 6061A. In the case of 6063B, the CMOD at peak force is notably reduced, whereas the peak force level is rather similar to 6063A. This might be partly attributed to the more ductile character of the 6063 alloy, but is most likely due to the slightly higher tensile strength of 6063B (see Fig. 4(a)), which could suffice to balance out a reduction in peak force that would otherwise be apparent if the tensile strength was similar between 6063A and 6063B. For the 6110 alloy, the peak force is somewhat reduced in the B-variants while the CMOD at peak force is comparable. These observations align well with results from Kahn tear tests recently reported by Qvale et al. [58].

Alloys 6061A and 6063A have the largest tensile ductility [57] and also display the most ductile character in the SE(B) tests — thus exhibit the highest toughness. Significant global plastic deformations have developed in 6061A and 6063A before peak force is reached, and the subsequent load drop is more gradual compared to the other alloys. In contrast, 6110A and all the B-variants exhibit negligible plastic deformations prior to peak force, followed by a rapid loss of load-carrying capacity. While the deviation between test repetitions in the post-peak deformation stage is somewhat larger in the A-alloys than in the B-alloys, the B-alloys have more scatter in the peak force values. This is reasonable since these materials display a more quasi-brittle behavior with much more confined plastic deformations. The scatter in the peak force values is most significant for 6110B, which has a difference of as much as 25% between the highest and lowest values. Note that the scatter of 6110B is probably exaggerated because of the lower initial stiffness observed in one of the three repeated tests on this alloy (see Fig. 6), and the current tests are therefore not conclusive in this respect. However, the recent results from Kahn tear tests reported by Qvale et al. [58] also show a higher degree of scatter for the 6110 alloys (see Fig. 4(b)), which corroborates the results of the current SE(B) tests. In general, the 6063 alloys exhibit the lowest degree of scatter in the SE(B) tests, which is consistent with the results from the Kahn tear tests.

Notable variation between test repetitions is observed for some of the alloys, which must be taken into account when the test data are analyzed. The SE(B) tests are governed by high-constraint loading
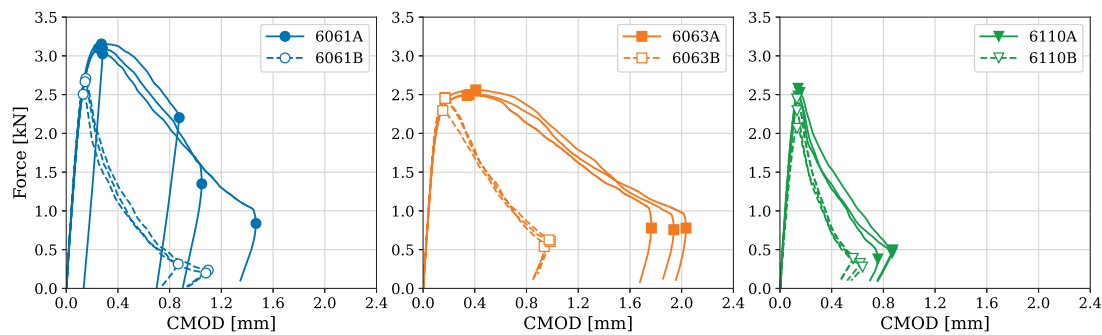
Fig. 6. Force-CMOD data from the three-point bending tests. Left-to-right: 6061, 6063, and 6110 alloys. The first marker on each graph highlights the peak force, whereas the second marker corresponds to the maximum CMOD obtained during the tests. Filled markers and solid lines are used for the A-variants, whereas open markers and dashed lines are used for the B-variants.

and even small variations in the initial specimen geometry may cause marked differences in the test results. The fatigue pre-cracking process, for instance, leads to small differences in the initial crack configuration between the test repetitions. The fatigue cracks are not straight and the fatigue crack tip was usually found to be slightly off-center, i.e. not directly below the indenter, such that crack initiation occurred under eccentric loading. The alloys with lowest ductility, i.e. the B-alloys, are more affected by such geometric deviations because the plastic zone ahead of the crack tip is more confined in those materials. This suggests that the larger scatter observed in the B-alloys might be partly attributed to differences in the fatigue crack configuration, or other geometric deviations, between test repetitions, and not only result from the alloys' intrinsic properties.

To facilitate a comparison with the work of Qvale et al. [58], we calculate the Unit Initiation Energy (UIE) and the Unit Propagation Energy (UPE) from the force–displacement data. These quantities are calculated from the mechanical energy divided by the initial area of the ligament up to peak force (UIE) and up to the point where we observe a 50%[2] drop in force level (UPE) in the softening stage, viz.

$$\text{UIE} = \frac{\int_0^{u_{\text{peak}}} F \, \mathrm{d}u}{A_{\text{lig}}}, \quad \text{UPE} = \frac{\int_{u_{\text{peak}}}^{u_{50\%\text{drop}}} F \, \mathrm{d}u}{A_{\text{lig}}} \tag{3}$$

where $A_{\text{lig}} = (W - a) \cdot B = 50$ mm^2 and u is the vertical displacement of the indenter. Note that the fatigue crack profile is not uniform over the specimen thickness and can vary slightly from specimen-to-specimen, so that A_{lig} must be regarded as a nominal value that for simplicity is assumed constant between all test specimens. Deviations from this assumption will affect the calculated values of UIE and UPE to some extent. The displacement of the moving crosshead is influenced by the compliance of the various components of the test rig, which leads to inaccurate measurements of the displacement of the rigid nose indenter. To obtain more accurate data for the vertical displacement of the specimens, we employed a point tracking algorithm to track the displacement of the indenter nose from the images recorded during each test. The point tracking algorithm was available through the in-house digital image correlation (DIC) software eCorr [64].

The mean UIE and UPE values, and the associated standard deviation, calculated from the SE(B) tests loaded beyond a 50% force drop are compiled in Table 3. Note that only two SE(B) tests were included in the calculations for 6061A, since one of the tests were unsuccessful and the others were stopped at higher force levels, whereas all other alloys include three repeat tests in the calculations of UIE and UPE. The mean values of UIE and UPE from the SE(B) tests are plotted against the area fraction of particles in Fig. 7, indicated by dashed lines and filled markers. The same quantities calculated from the Kahn test data

of Qvale et al. [58] are also plotted to facilitate a comparison between the two different test configurations, and these are indicated by dotted lines and open markers.

Both UIE and UPE are significantly reduced for the B-alloys in the SE(B) tests. Based on the mean values from Table 3, the reduction of UIE and UPE in the B-alloys is respectively 55% and 84% for 6061, 60% and 70% for 6063, and 21% and 55% for 6110. It thus transpires that 6061B and 6063B exhibit a larger reduction in both UIE and UPE than alloy 6110B, and are consequently more affected by the increased particle content. This is also readily seen from the graphs in Fig. 7. The larger reduction of UIE and UPE for the 6061 and 6063 alloys is related to the transition from a more ductile character of the A-alloys to a quasi-brittle character of the B-alloys (see Fig. 6 for reference), whereas both 6110A and 6110B appear quasi-brittle in the SE(B) tests. The effect of increasing the particle content is thus less prominent for the 6110 alloy. It must be emphasized that this does not imply a superior behavior of the 6110 alloy – in fact rather the opposite – but is a manifestation of the comparatively poor properties of the 6110A alloy. A somewhat different result is observed in the Kahn tests, where the reduction in both UIE and UPE for the B-alloys is comparable between all three alloy groups (see Fig. 7). It thus seems that the stress triaxiality levels attained in the SE(B) tests are sufficiently high to promote quasi-brittle behavior of the 6110A alloy, while the stress triaxiality is too low for this to occur in the Kahn tearing tests, and consequently neither in the tensile tests reported by Tomstad et al. [57].

4.2. Crack topology rendered by XCT

Crack profiles and corresponding force–CMOD plots from the scanned test specimens are shown in Figs. 8 and 9. In these figures, the red and blue rectangles shown to the right and below the 3D crack surfaces are cross-sectional views of the crack surface on planes that are parallel (red) and perpendicular (blue) to the crack propagation direction. The longest edge of each rectangle corresponds to the specimen width (red rectangles) or the specimen thickness (blue rectangles). Markers highlighted on the force–CMOD graphs indicate the end of the tests.

Different stages of crack propagation are indicated by the crack surfaces depicted in Fig. 8, which correspond to three different levels of global deformation. Note that these crack profiles were rendered from three unique test samples (Test 1–3 in the figure) and consequently do not depict various stages of the *same* crack. As indicated by the plotted force–CMOD curves, the first test was stopped shortly after peak load, whereas the second and third tests were stopped at larger deformations. In Test 1, the crack has already propagated slightly, but the crack profile still closely resembles the shape of the initial fatigue crack. The crack advances through the central region of the specimen first, i.e. crack tunneling, due to the prevailing plane strain conditions [45,51]. When the external loading is increased to deformation levels between Test 2 and Test 3, shear lips develop towards the

---

[2] UPE is usually calculated for larger deformations, e.g. where the load is reduced to 5% of the peak force or lower, but the unsuccessful test on 6061A necessitated a higher threshold to include more than one test in the calculation.

Table 3
UIE and UPE calculated from the SE(B) tests given in terms of mean value and standard deviation.

Alloy	6061A	6061B	6063A	6063B	6110A	6110B
UIE [kJ/m^2]	18.63 ± 1.59	8.30 ± 0.83	22.52 ± 2.23	9.04 ± 0.76	8.05 ± 0.72	6.38 ± 0.64
UPE [kJ/m^2]	41.99 ± 0.51	6.89 ± 0.56	55.65 ± 2.47	16.50 ± 0.08	10.48 ± 1.02	4.68 ± 0.20
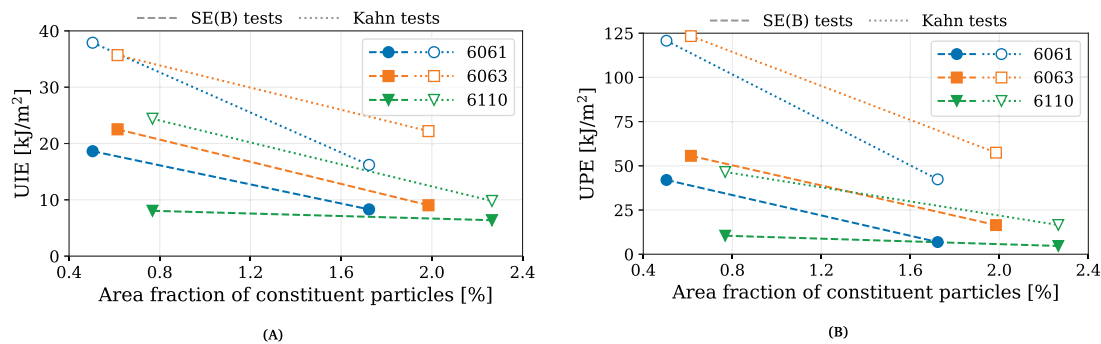
Fig. 7. (A) UIE and (B) UPE plotted vs. the area fraction of particles obtained from SEM images. Filled markers pertain to A-alloys and open markers pertain to B-alloys. Dotted and dashed lines are plotted between the A-variant and the B-variant of the same alloy to aid the interpretation.
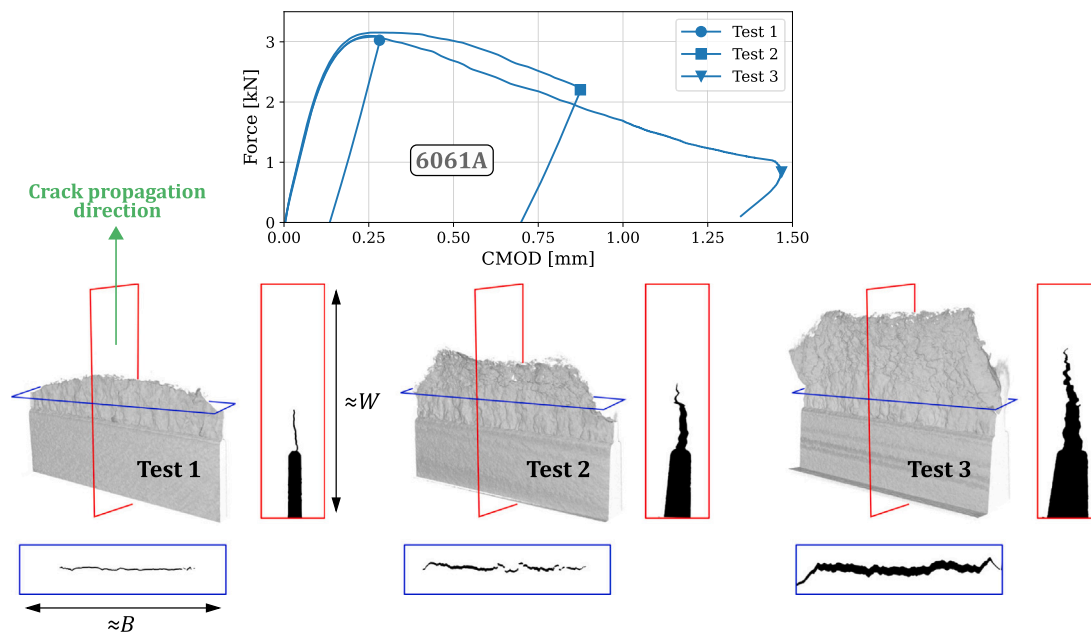
Fig. 8. Evolution of the crack surface during loading. Force-CMOD data for the test specimens used in the XCT analyses are plotted in the upper figure.

outer surfaces of the specimens where the stress triaxiality is lower and results in through-thickness fracture some distance into the specimen. This mixed-mode fracture behavior of ductile materials in SE(B) tests is well-known (e.g. Hahn et al. [65] and Knott [66]). The prevalence of shear lips can be reduced using side-grooved specimens, which diminishes the plane stress region and leads to a more uniform crack extension (e.g. Delorenzi and Shih [67] and Poulose [68]).

The crack surface in extensively deformed specimens for all six alloys are depicted in Fig. 9. The top row of crack profiles corresponds to A-variants and the bottom row corresponds to B-variants, while images from left-to-right pertain to alloys 6061, 6063, and 6110. Note that the various specimens were deformed to different levels of force and displacement, as inferred from the markers highlighted in the force–CMOD curves in Fig. 9, and the crack surfaces consequently only facilitate a qualitative comparison of the alloys. We readily see that the crack has propagated farther into the specimens in the B-variants than in the A-variants, which is corroborated by the lower unloading stiffness at the end of each test in the B-variants. This explains the rapid

loss of load-carrying capacity, and consequently lower toughness, in the B-alloys. The crack front also appears more uniform, and the prevalence of the shear lips seems somewhat less, in the B-alloys. However, the crack profiles in 6110A and 6110B are rather similar, which is in agreement with the similarity between the force–CMOD curves (see Section 4.1) of these two alloys.

4.3. Grain structure images deformed specimens

Grain structure images from the mid-section of the test specimens used in the XCT analysis are shown in Figs. 10(a), 10(b), and 10(c) for the 6061, 6063, and 6110 alloys, respectively. A magnified view of the crack tip region in the same specimens is shown in Fig. 11. The images were prepared using an overlay of grain structure images and regular light microscope images to ease the interpretation of how the crack propagates within the material microstructure (see Section 3.3).

The XCT images (Figs. 8 and 9) show that the crack has a jagged profile but is nominally flat in the central part of the specimen in all
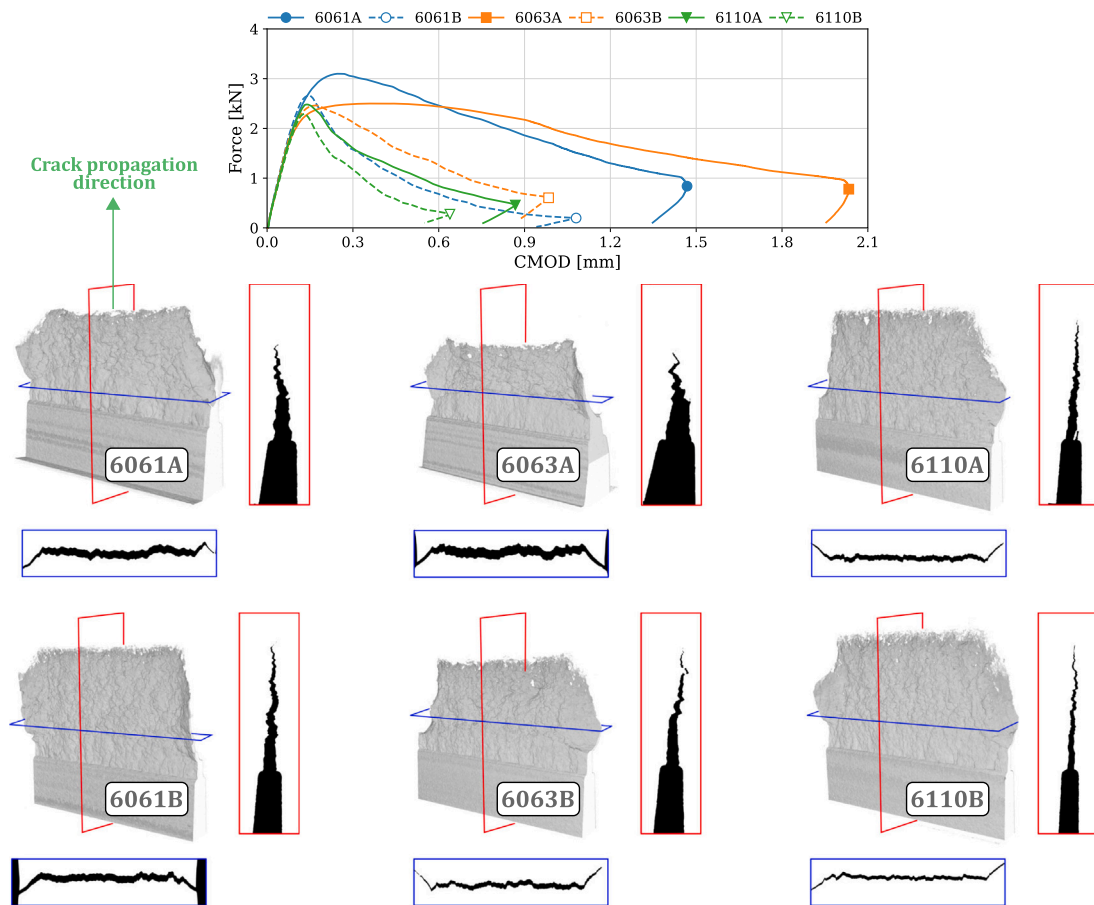
Fig. 9. Crack profiles in heavily deformed specimens. From left-to-right: 6061, 6063, and 6110. A-alloys are shown in top row and B-alloys in bottom row. Force-CMOD data for the test specimens used in the XCT analyses are plotted in the upper figure.
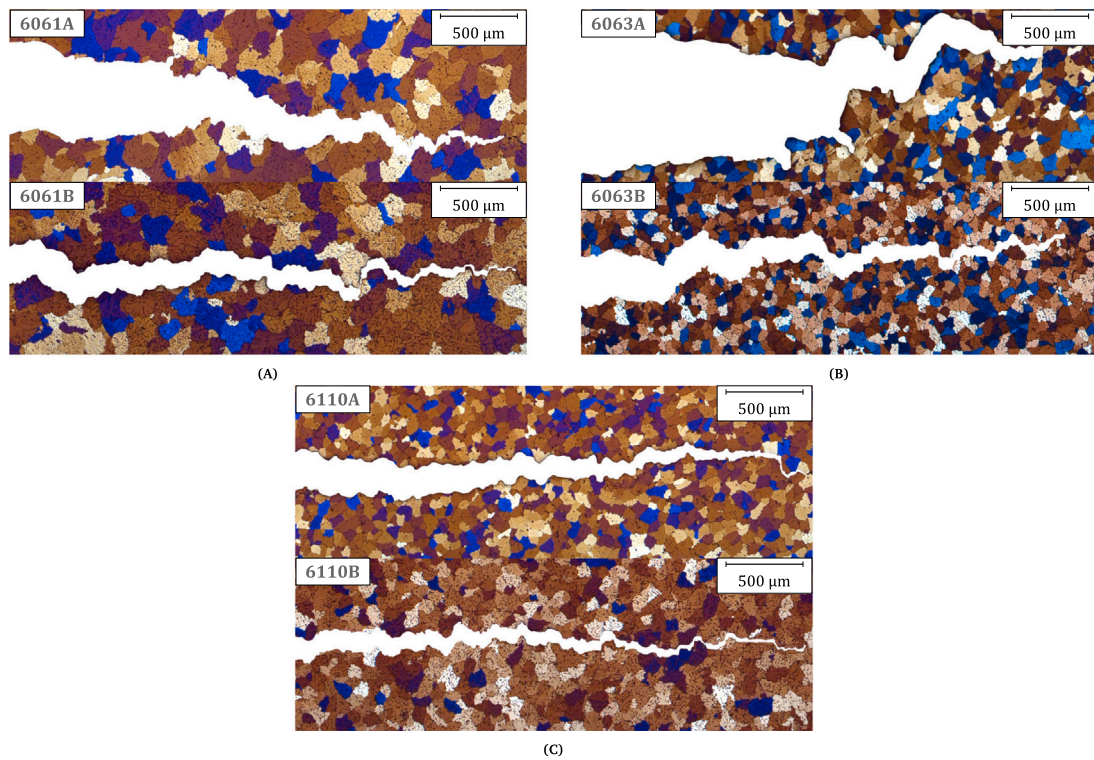

Fig. 10. Grain structure and crack path in deformed test specimens: (A) 6061 alloys, (B) 6063 alloys, and (C) 6110 alloys. Images were taken at a 50x magnification.
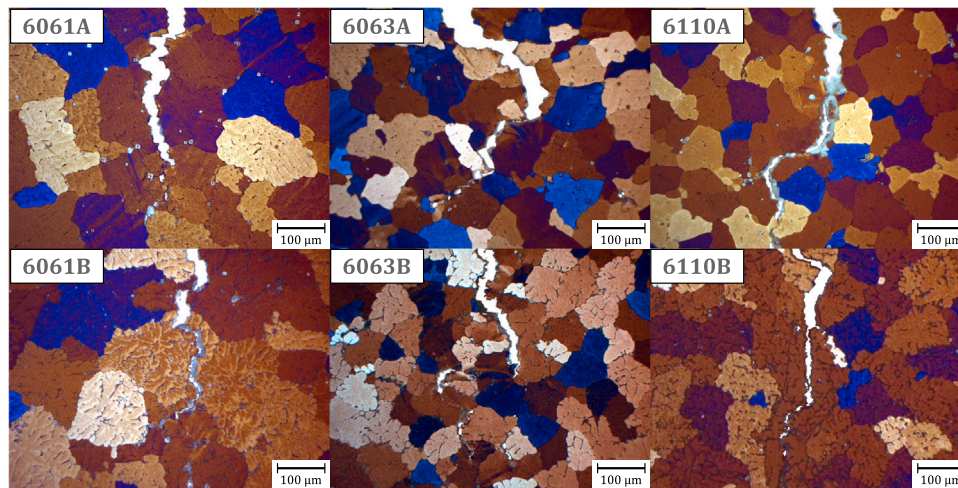
Fig. 11. Grain structure close to the crack tip in deformed test specimens. Images were taken at a 200x magnification.

alloys. The grain structure images shown in Fig. 10 corroborate this observation, where the cracks are seen to propagate in a zig-zag pattern along a nominally rather straight path through the crack ligament. The zig-zag pattern results from a competition between the strain localization occurring in bands inclined at about 45° from the crack plane, the global constraints, and the local constraints imposed by the grain and dendrite arm boundaries. These competing effects are reconciled by allowing the crack to deviate slightly from the nominally straight path. The cracks tend to follow the particle-rich grain and dendrite arm boundaries, as they are primary sites for void nucleation. Since the grain and dendrite arm boundaries are numerous and randomly oriented, the probability that one such interface is oriented about 45° from the crack plane is quite high.

The cracks propagate both by transgranular and intergranular modes, which is perhaps most easily observed from the grain images corresponding to the 6061 alloys (Fig. 10(a)) due to their larger grain size. Closer examination of the magnified views around the crack tip shown in Fig. 11 reveals that the regions exhibiting transgranular fracture characteristics correspond to dendrite arm boundaries, in which constituent particles tend to cluster after solidification (see Section 2.2). Thus, crack propagation takes place along interfaces where the area fraction of constituent particles is high – either on high-angle grain boundaries or on the dendrite arm boundaries – in these as-cast alloys; at least under the prevailing high stress triaxiality loading conditions.

5. Discussion

Variations in the ductility and toughness of metal alloys may have different physical origins. In terms of macroscopic properties, an alloy's strength and work-hardening capacity are usually considered to be important factors, whereas the grain size and morphology, particle size, shape, and spacing, and precipitate-free zones are among the microscopical properties that could prove decisive for the ductile fracture process. This work is mainly aimed at an assessment of the effects related to the constituent particles. Addition of Si and Fe to the A-variants increased the content of constituent particles in the B-variants by a factor of 3.42 in 6061, 3.23 in 6063, and 2.94 in 6110. Only minor differences in the hardening rate and strength were found between the A-variant and the B-variant of each alloy, with the largest difference observed between the 6063 alloys (ref. Fig. 4(a)). Other microstructural parameters (e.g. particle size, particle shape, and grain size) were largely unaltered, but the most notable variation was found between 6061A and 6061B where the grain size was reduced and the particle size was increased in the latter. Also the chemical composition of the particles and the matrix surrounding them are assumed to be similar between the alloys, so the nucleation properties should be the same in all alloys. Differences between the A-variants and the B-variants are therefore assumed to derive mainly from variations in the amount and distribution of constituent particles. However, note that the strength and work hardening and the microstructure vary between the three alloy types, i.e. between 6061, 6063, and 6063, which enables a qualitative assessment of their relative impact on ductility and toughness of the alloys tested herein.

Increasing the strength or lowering the work hardening capacity is normally considered negative for the ductility and toughness [10,31, 32,35,36]. With respect to the strength, this aligns with the observed trends between the 6063 and 6110 alloys, where the 6110 alloys have a higher strength but much lower ductility and toughness than the 6063 alloys (see Figs. 4 and 6). In general terms, however, there seems to be no correlation between the strength and hardening capacity and the ductility and toughness of these alloys. This is readily seen by comparing the flow stress curves and the hardening data plotted in Fig. 12 with the values of UIE and UPE listed in Table 3. For instance, the 6110A alloy has nearly the same hardening capacity as 6061A, but only half the ductility and less than half of the toughness of 6061A. Also, 6063A has the lowest hardening capacity of all alloys, but still exhibits the highest ductility and toughness. In terms of the trade-off between strength and fracture resistance [36], the behavior of 6061A is in fact quite remarkable, having a similar strength as 6110A while maintaining a ductility, tearing resistance, and toughness comparable to 6063A (cf. Figs. 4 and 7). This advantageous property of the 6061 alloy seems to be nearly lost when the constituent-particle content is increased (see results for 6061B), for which the strength is still as high but the ductility and toughness is markedly reduced. Clearly, macroscopic properties such as strength and hardening capacity cannot uniquely account for the differences in damage resistance between these six alloys.

The SE(B) tests clearly show that an increased content of constituent particles inflicts poor toughness properties in these alloys. The force–CMOD data and energy data plotted in Figs. 6 and 7 show that the peak force level attained in the tests, the CMOD at peak force, and both UIE and UPE were consistently reduced in the B-variants. While 6061A and 6063A display a ductile character, with notable plastic deformations taking place before peak force is reached, 6110A and all the B-variants exhibit very limited ductile behavior in the global response curves and suffer from a rapid loss of load-carrying capacity. Crack propagation thus takes place more easily in the B-alloys. The combination of a rather low ductility and a high stress triaxiality ahead of the crack tip reduces the size of the fracture process zone and gives rise to a quasi-brittle character of the B-alloys.
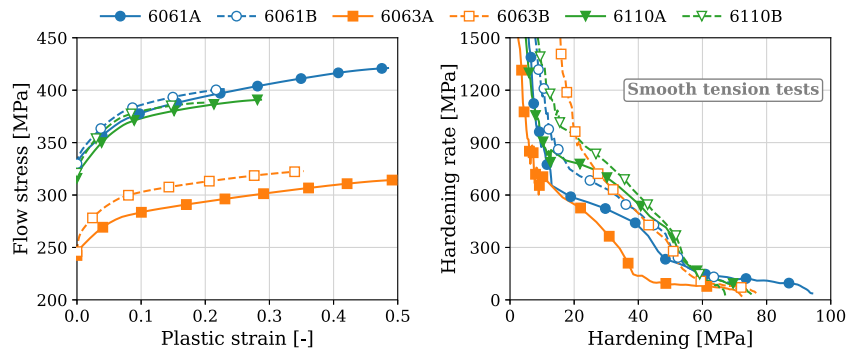
Fig. 12. Flow stress curves and Kocks–Mecking plots for all alloys based on tests on smooth axisymmetric samples.

Table 4

Estimates of local particle fraction (f_{gb}) and particle spacing ($\bar{d}_{gb}$) based on a simplified analysis using the expression in Eq. (4) and the microstructural parameter values listed in Table 2.

Alloy	6061A	6061B	6063A	6063B	6110A	6110B
f_{gb}	0.35	0.73	0.14	0.40	0.17	0.63
$\bar{d}_{gb}$ [µm]	1.00	0.92	2.54	1.51	2.45	1.16

The 6061 alloy seems to be most influenced by an increase of the constituent-particle content, as it exhibits the largest differences in the force–CMOD curves between the A-variant and the B-variant, i.e. largest reduction in peak force, CMOD at peak force, and toughness. One potential reason for this is the difference in mean grain size and mean particle size between 6061A and 6061B (6061B has larger particles and smaller grains on average than 6061A), whereas both the particle size and the grain size are similar in the 6063 and 6110 alloys (ref. Table 2). Conflicting results have been reported regarding the influence of grain size on toughness (e.g. [6,69]), and considering the similar grain size of the 6063 and 6110 alloys – but very different ductility and toughness – it is considered less likely that the grain size has an explicit effect on the ductility and toughness in these alloys. Note that the dendrite arm spacing and size may also impact the toughness [70], but these parameters have larger impact on the properties of cast alloys (in the current study we examine *wrought* alloys in an as-cast and homogenized state) where the inter-dendritic regions constitute a much larger volume fraction. A more likely reason for the large difference between 6061A and 6061B is that the difference in particle content between the A-variant and the B-variants is larger for 6061 than for 6063 and 6110, and additionally that the particles are larger in 6061B than in 6061A. It transpires that the ductility and toughness of these alloys are primarily governed by the constituent particles. The influence of the constituent particles is, however, not only related to the volume fraction of these particles, but also to their size, shape, and spatial distribution.

Figs. 10 and 11 show that crack propagation occurs primarily at the grain boundaries and dendrite arm boundaries in the regions governed by plane strain conditions, i.e. towards the center of the specimen. Fracture thus occurs by void nucleation, growth and coalescence from the constituent particles at these interfaces. High stress triaxiality loading has been found to increase the propensity for intergranular fracture in materials where the matrix is separated by softer zones [35], which gives rise to local concentrations of stresses and strains. This is in some sense similar to the type of property mismatch induced by grain boundaries and dendrite arm boundaries in the current alloys. Strain localization analyses based on the imperfection-band approach [71] have clearly demonstrated how material imperfections set limits to the failure strain (e.g. [72–75]). Deshpande et al. [76] noted that cracks would advance by intergranular fracture when there is a high probability of finding a grain segment perpendicular to the loading direction. The near radial symmetry of the PCF plots in Fig. 3 shows

that the particle clusters are quite randomly distributed in the six aluminum alloys examined in the current study. We may therefore assume that the grain boundaries and dendrite arm boundaries exhibit a random orientation on average, and considering that the grains and dendrite arms exist in large numbers in these alloys, it is a rather high probability of sampling a particle-containing interface in a favorable orientation close to the crack tip. Plastic strains will concentrate in bands oriented at around 45° to the crack plane, which thus seems a favorable orientation for crack extension. However, global constraints set by specimen geometry and loading conditions promote a straight crack path normal to the loading direction, and the crack thus advances in a zig-zag pattern to reconcile these two competing effects. This causes the jagged fracture surface observed from the XCT images and the grain images of the deformed samples shown in Sections 4.2 and 4.3.

All alloys have constituent particles arranged in short-range clusters at dendrite arm boundaries and grain boundaries, and there is consequently no apparent difference between these alloys in terms of the spatial distribution of the constituent particles. However, this implies that the density of grain boundaries (i.e. grain size) and dendrite arm boundaries exerts an influence on the local area fraction of particles and the mean particle spacing. The area fraction of particles can be significantly higher, and the particle spacing can be significantly lower, if the particles are clustered along these interfaces, as inferred from the SEM image shown in Fig. 13. The SEM image is adapted from the work of Tomstad et al. [57]. The toughness of aluminum alloys has been found to decrease significantly when the fraction of grain boundary particles increases [77–79]. Nakai and Eto [80] reported that the fracture toughness was proportional to the square root of the particle spacing from tests on a 2024 aluminum alloy, and found that the fracture toughness increased by 20% when the particle spacing changed from 75 µm to 140 µm. Similar effects could also be important for the aluminum alloys used in the current study.

To qualitatively examine how this short-range clustering affects the local particle fraction and particle spacing, we make a simplified analysis assuming that all particles are confined to the grain boundaries, rather than being homogeneously distributed throughout the grain. Note that the dendrite arms within the grains (ref. Fig. 1) are not accounted for in this simplified analysis. We assume that the grains and particles are cubic with characteristic sizes equal to D_g and D_p, respectively, and that each grain boundary is shared by two grains. Each of the six faces of the grain thus contain $1/3$ of the N_p number of constituent particles. If the particles are further assumed to be uniformly distributed along the grain boundaries, i.e. the particle spacing is constant, the local area fraction of constituent particles (f_{gb}) and the mean particle spacing at the grain boundaries ($\bar{d}_{gb}$) may be expressed as

$$f_{gb} = \frac{1}{3}\frac{D_g}{D_p}f_p, \qquad \bar{d}_{gb} = \sqrt{3}f_p^{-\frac{1}{2}}D_g^{-\frac{1}{2}}D_p^{\frac{3}{2}} \qquad (4)$$
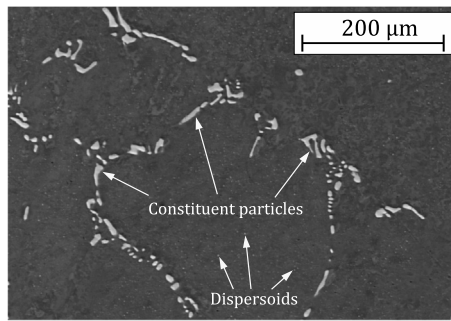
Fig. 13. SEM image of particles in 6110B. The large constituent particles are seen to arrange in short-range clusters while small dispersoids (small dots) are distributed evenly throughout the grains. The SEM image was acquired as part of the study by Tomstad et al. [57].

where f_p, D_p, and D_g refers to the particle fraction, particle size, and grain size determined from the microstructural characterization (see Section 2.2). It must be stressed that this analysis, and consequently also the expressions in Eq. (4), is highly approximate and based on idealizations that do not correctly represent the material microstructure. Note that the expression for f_{gb} can be written on a form similar to that reported in Bourcier et al. [81], i.e. $f_{gb} = k f_p^{2/3}$, if the parameter k is equal to $\sqrt[3]{N_p}/3$.

If the microstructural data compiled in Table 2 are inserted in these expressions, we obtain the values listed in Table 4. Even though these values are clearly exaggerated and should not be used quantitatively, they still facilitate a qualitative interpretation of the particle clusters, as inferred from Fig. 13, and can therefore rationalize some of the trends in ductility and toughness properties of these alloys. For instance, the relatively high toughness of 6063A can be understood as a combination of its lower strength, that it has the lowest estimated area fraction of particles, and that it has the largest ratio $\bar{d}_{gb}/D_p$ between estimated particle spacing and particle size (cf. Tables 2 and 4). Similar arguments may be used for the 6063B alloy in comparison with the other B-alloys. Another example is the difference between 6061A and 6061B, which is found to be larger than between the A-variant and B-variant of the two other alloys. This could be caused by the combination of (i) a larger mean particle size in 6061B, (ii) that the 6061 alloy has the largest increase in particle content between the A- and B-variant (as previously discussed), and (iii) that the local particle spacing is very small, and quite similar to the mean particle size, in 6061B (cf. Tables 2 and 4). The latter implies that the inter-particle ligament size is drastically reduced. In turn, this intensifies the stress concentration and increases the void nucleation rate, and additionally increases the propensity for strain localization between neighboring voids, which expedites void coalescence — in the extreme case, void coalescence occurs nearly simultaneously with nucleation. On the contrary, 6061A has both larger mean spacing and smaller particles, which increases the inter-particle ligament size. This combination could be a primary reason for the outstanding properties of 6061A, but it should be noted that 6061A still has a quite large area fraction of particles according to the estimate of this simple analysis. The smaller particle size therefore seems to be a more viable explanation for the relatively high ductility and toughness of 6061A.

The much lower ductility and toughness of the 6110 alloy compared to the other alloys cannot be explained from the simplified analysis presented above. For instance, the estimated values listed in Table 4 above entail that the particle spacing is much higher in 6110A than in 6061A, and that the estimated area fraction of particles is generally less in the 6110 alloy than in the 6061 alloy. Both these effects should increase the toughness, but the opposite is observed in the SE(B) tests. Of course, the premises of the simplified analysis presented above were at best approximate. There are several aspects that may either

independently or jointly inflict the poor toughness of the 6110 alloy (cf. Table 2 and Fig. 4):

- high strength (comparable to 6061),
- highest particle content,
- largest mean particle size (comparable to 6063),
- largest standard deviation (calculated from the particle measurements), i.e. the widest range of particle sizes,
- small grains (comparable to 6063), and
- highest Mn-content.

High strength and high stress triaxiality will both increase the maximum principal stress and thereby expedite the void nucleation process [9,30,82,83], after which the high stress triaxiality leads to rapid void expansion and imminent void coalescence. As such, the 6110 alloy adheres to the commonly reported trade-off between strength and toughness. Further, the fraction of broken particles has been found to increase markedly with increasing particle size in various 6xxx aluminum alloys [10], which implies that larger particles have a higher propensity for void nucleation. Since the 6110 alloy both has high strength and relatively large particles, these two effects may jointly be responsible for the large differences in ductility, tearing resistance, and toughness between 6061 and 6110 (cf. Figs. 4 and 7). Generally speaking, both the high particle content and the smaller grain size of the 6110 alloys will tend to lower the particle spacing, although this is partly counteracted by the larger particle size, as inferred from the values in Table 4. A wider range of particle sizes may also increase the void nucleation rate [50], but this is not believed to have a large effect for the alloys here since the standard deviation of the particle size measurements is not significantly different between the alloys.

It is somewhat puzzling that 6110A has a lower toughness than 6063B, and comparable to 6061B, even though the constituent-particle content is less than half in the former. This observation is difficult to rationalize based on what has been discussed previously. The much higher Mn-content in the 6110 alloys is a conceivable reason, since it leads to the formation of a rather uniform distribution of small dispersoids throughout the grains, as shown for the 6110B alloy in Fig. 13. As mentioned in the Introduction, conflicting observations have been reported regarding the dispersoids' influence on ductility and toughness in metals (e.g. Blind and Martin [11] and Liu et al. [12,13]). They have both been found to increase the toughness, presumably by causing a more homogeneous plastic slip distribution or by causing a transition from intergranular to transgranular fracture, and to lower the toughness, mainly by promoting void-sheeting. Walsh et al. [37] found that the Mn-content had a pronounced effect on the ductility and toughness of a 2134 aluminum alloy with four different levels of Mn. Up to a certain (critical) value, addition of Mn led to the formation of slip-distributing dispersoids that increased the ductility, but increasing the content of Mn beyond this point only led to the formation of larger Mn-rich primary particles that lowered the ductility. The chemical composition of the constituent particles analyzed by Thomesen et al. [26] suggest that they have a composition close to $Al_{50}(Fe,Mn,Cr)_{12}Si_7$. A part of the Mn content is therefore tied up in these constituent particles, while the remaining Mn atoms form smaller dispersoids or other types of Mn-rich particles. Based on the chemical composition (ref. Table 1), the 6061 and 6063 alloys are not expected to form dispersoids, whereas a high amount of dispersoids are expected to form in the 6110 alloys. Considering that both 6110A and 6110B exhibit poor toughness, it is difficult to advocate a positive effect of the dispersoids on the toughness. However, there are no obvious signs that the dispersoids affect the toughness negatively either, since all alloys were found to mainly fracture along the grain and dendrite boundaries, while the dispersoids are distributed in the grain interior (Fig. 13). It transpires that the dispersoids have no apparent influence on toughness in these alloys, but it must be noted that this conclusion is strongly related to the as-cast state of the alloys where the constituent particles are clustered along grain and dendrite arm boundaries. This imposes strong constraints

for crack propagation and governing fracture mechanisms, which are alleviated for instance in extruded alloys where the constituent particles are re-distributed to the grain interior. In the latter case, the dispersoids might have a larger influence on fracture resistance, but this is outside the scope of the current study.

Many of the observed trends in the SE(B) tests can be explained based on the microstructural properties, in combination with the material strength, and the results from the SE(B) tests corroborate conclusions from the previous studies on the same alloys [57,58]. It is still, however, difficult to account for the large discrepancy between 6061A and 6110A based on the currently available data. Differences in particle size might be the main reason, provided that the particle size in these alloys is sufficiently different to change the nucleation rate quite markedly. Another viable candidate for causing these differences is precipitate-free zones (PFZs), as for instance recently studied in a similar aluminum alloy by Arani et al. [84], which are present in the aluminum alloys considered here (see e.g. [85]). The PFZs are softer than the surrounding grains, which can lead to significant strain localization (see e.g. [84,86]), and have the largest influence for the peak-aged condition (temper T6) where the strength is highest. Based on an idealized finite element model of the PFZ, Pardoen et al. [87] found that the effects of PFZs on failure in aluminum alloys were most pronounced when (i) the material is subjected to high stress triaxiality loading conditions, (ii) the voids are closely spaced, and (iii) the PFZs are quite thick compared to the void size. The two former factors are clearly relevant in the current context and imply that PFZs may affect the failure process in these alloys. However, a detailed assessment of the PFZs' influence on failure requires detailed material characterization using transmission electron microscopy (TEM) and is outside the scope of the current work.

6. Concluding remarks

This study has examined the effects of constituent-particle content on the fracture of three 6000-series aluminum alloys under high-constraint loading conditions. Single-edge-notch bending tests on specimens with a fatigue crack were performed to enforce high stress triaxiality loading conditions at the crack tip. All alloys were artificially aged to temper T6. To isolate effects of the constituent particles, each of the three alloy types was manufactured with two different volume fractions of constituent particles. One variant (A-alloy) corresponded to the commercial alloy type, whereas the second (B-alloy) was manufactured with a higher amount of Fe and Si. This increased the amount of constituent particles, while the grain structure, strength, and work hardening were largely unaltered.

The SE(B) tests clearly showed that an increased content of constituent particles reduces the fracture resistance in these 6000-series aluminum alloys. Strength was found to influence the toughness, but the results of 6061A and 6110A showed that there is no monotonic relation between these two parameters. This contradicts the commonly reported trade-off between strength and toughness, and implies that strength is not always the most decisive factor for ductility and toughness in these alloys. The toughness is primarily affected by the constituent-particle content, the particle size, and the spacing between the particles. The B-alloys and the 6110A alloy exhibited a quasi-brittle character, whereas 6061A and 6063A displayed a somewhat more ductile character. This was confirmed by the fracture energy values calculated from force–CMOD data in the tests, represented here in terms of UIE and UPE. The constituent particles were found to mainly reside at the grain boundaries and the dendrite arm boundaries within the grains and these interfaces were found to be preferential sites for crack propagation in the specimen center, regardless of the alloy type and constituent-particle content. Fracture in the SE(B) tests was consequently governed by continuous void nucleation, growth, and coalescence from constituent particles at grain boundaries and dendrite arm boundaries for all six alloys. Previous studies by Tomstad et al.

[57] and Qvale et al. [58] have demonstrated that an increase of the constituent-particle content is detrimental for the ductility and tearing resistance of these materials. Based on the results from the SE(B) tests performed in the current study, it is concluded that the constituent particles have an even larger influence on the fracture resistance of these materials when the stress triaxiality increases.

CRediT authorship contribution statement

Lars Edvard Blystad Dæhli: Conceptualization, Methodology, Data curation, Formal analysis, Resources, Investigation, Visualization, Writing – original draft, Writing – review & editing. **Sindre Nordmark Olufsen:** Conceptualization, Data curation, Visualization, Writing – review & editing. **Tore Andre Kristensen:** Resources, Investigation. **Tore Børvik:** Conceptualization, Writing – review & editing, Funding acquisition. **Odd Sture Hopperstad:** Conceptualization, Methodology, Writing – review & editing, Project administration, Funding acquisition.

Declaration of competing interest

The authors declare that they have no known competing financial interests or personal relationships that could have appeared to influence the work reported in this paper.

Data availability

Data will be made available on request.

Data availability

The raw/processed data required to reproduce these findings cannot be shared at this time as the data also form parts of an ongoing study. However, the data used to support the findings of this study are available from the corresponding author upon request.

References

[1] P.J. Noell, J.D. Carroll, B.L. Boyce, The mechanisms of ductile rupture, Acta Mater. 161 (2018) 83–98, http://dx.doi.org/10.1016/j.actamat.2018.09.006, URL: https://doi.org/10.1016/j.actamat.2018.09.006https://linkinghub.elsevier. com/retrieve/pii/S1359645418307006https://www.sciencedirect.com/science/ article/pii/S1359645418307006?dgcid=raven_sd_aip_email.

[2] W. Garrison, N.R. Moody, Ductile fracture, J. Phys. Chem. Solids 48 (11) (1987) 1035–1074, http://dx.doi.org/10.1016/0022-3697(87)90118-1.

[3] A.A. Benzerga, J.B. Leblond, Ductile fracture by void growth to coalescence, Adv. Appl. Mech. 44 (2010) 169–305, http://dx.doi.org/10.1016/S0065-2156(10)44003-X.

[4] H. Toda, H. Oogo, K. Horikawa, K. Uesugi, A. Takeuchi, Y. Suzuki, M. Nakazawa, Y. Aoki, M. Kobayashi, The true origin of ductile fracture in aluminum alloys, Metall. Mater. Trans. A 45A (2014) 765–776, http://dx.doi.org/10.1007/s11661-013-2013-3.

[5] A.J. Gross, K. Ravi-Chandar, On the deformation and failure of al 6061-T6 in plane strain tension evaluated through in situ microscopy, Int. J. Fract. (2017) 1–26, http://dx.doi.org/10.1007/s10704-017-0209-z.

[6] G.T. Hahn, A.R. Rosenfield, Metallurgical factors affecting fracture toughness of aluminum alloys, Metall. Trans. A 6 (4) (1975) 653–668, http://dx.doi.org/10.1007/BF02672285.

[7] J. Hancock, A. Mackenzie, On the mechanisms of ductile failure in high-strength steels subjected to multi-axial stress-states, J. Mech. Phys. Solids 24 (2–3) (1976) 147–160, http://dx.doi.org/10.1016/0022-5096(76)90024-7, URL: https://linkinghub.elsevier.com/retrieve/pii/0022509676900247.

[8] F.M. Beremin, Cavity formation from inclusions in ductile fracture of A508 steel, Metall. Trans. A 12 (5) (1981) 723–731, http://dx.doi.org/10.1007/BF02648336, URL: http://link.springer.com/10.1007/BF02648336.

[9] A. Pineau, A. Benzerga, T. Pardoen, Failure of metals I – brittle and ductile fracture, Acta Mater. 107 (2016) 424–483, http://dx.doi.org/10.1016/j.actamat.2015.12.034, URL: https://linkinghub.elsevier.com/retrieve/pii/S1359645415301403.

[10] F. Hannard, T. Pardoen, E. Maire, C.L. Bourlot, R. Mokso, A. Simar, Characterization and micromechanical modelling of microstructural heterogeneity effects on ductile fracture of 6xxx aluminium alloys, Acta Mater. 103 (2016) 558–572, http://dx.doi.org/10.1016/j.actamat.2015.10.008.

[11] J. Blind, J. Martin, The effect of dispersoids on the ductile fracture toughness of Al–Mg–Si alloys, Mater. Sci. Eng. 57 (1) (1983) 49–54, http://dx.doi.org/10.1016/0025-5416(83)90026-5, URL: https://linkinghub.elsevier.com/retrieve/pii/0025541683900265.

[12] G. Liu, G.J. Zhang, X.D. Ding, J. Sun, K.H. Chen, Dependence of fracture toughness on multiscale second phase particles in high strength Al alloys, Mater. Sci. Technol. 19 (7) (2003) 887–896, http://dx.doi.org/10.1179/026708303225004314.

[13] G. Liu, G.J. Zhang, X.D. Ding, J. Sun, K.H. Chen, The influences of multiscale-sized second-phase particles on ductility of aged aluminum alloys, Metall. Mater. Trans. A 35 A (6) (2004) 1725–1734, http://dx.doi.org/10.1007/s11661-004-0081-0.

[14] G. Liu, S. Scudino, R. Li, U. Kühn, J. Sun, J. Eckert, Coupling effect of primary voids and secondary voids on the ductile fracture of heat-treatable aluminum alloys, Mech. Mater. 43 (2011) 556–566, http://dx.doi.org/10.1016/j.mechmat.2011.06.014.

[15] M.H. Mulazimoglu, A. Zaluska, J.E. Gruzleski, F. Paray, Electron microscope study of Al-Fe-Si intermetallics in 6201 aluminum alloy, Metall. Mater. Trans. A 27 (4) (1996) 929–936, http://dx.doi.org/10.1007/BF02649760, URL: https://link.springer.com/10.1007/BF02649760.

[16] A.L. Dons, The alstruc homogenization model for industrial aluminum alloys, J. Light Metals 1 (2) (2001) 133–149, http://dx.doi.org/10.1016/S1471-5317(01)00007-4.

[17] M.S. Remøe, K. Marthinsen, I. Westermann, K.O. Pedersen, J. Røyset, C. Marioara, The effect of alloying elements on the ductility of Al-Mg-Si alloys magnus, Mater. Sci. Eng. A693 (March) (2017) 60–72, http://dx.doi.org/10.1007/s11947-009-0181-3.

[18] S. Zajac, B. Hutchinson, A. Johansson, L.-O. Gullman, Microstructure control and extrudability of Al–Mg–Si alloys microalloyed with manganese, Mater. Sci. Technol. 10 (4) (1994) 323–333, http://dx.doi.org/10.1179/mst.1994.10.4.323.

[19] A.L. Dons, E.K. Jensen, Y. Langsrud, E. Trømborg, S. Brusethaug, The alstruc microstructure solidification model for industrial aluminum alloys, Metall. Mater. Trans. A 30 (8) (1999) 2135–2146, http://dx.doi.org/10.1007/s11661-999-0025-9.

[20] N.C. Kuijpers, J. Tirel, D.N. Hanlon, S. Van der Zwaag, Quantification of the evolution of the 3D intermetallic structure in a 6005A aluminium alloy during a homogenisation treatment, Mater. Charact. 48 (5) (2002) 379–392, http://dx.doi.org/10.1016/S1044-5803(02)00289-9.

[21] K.B.S. Couto, S.R. Claves, W.H. Van Geertruyden, W.Z. Misiolek, M. Goncalves, Effects of homogenisation treatment on microstructure and hot ductility of aluminium alloy 6063, Mater. Sci. Technol. 21 (2) (2005) 263–268, http://dx.doi.org/10.1179/174328405X18584, URL: http://www.tandfonline.com/doi/full/10.1179/174328405X18584.

[22] D. Lassance, D. Fabrègue, F. Delannay, T. Pardoen, Micromechanics of room and high temperature fracture in 6xxx Al alloys, Prog. Mater. Sci. 52 (1) (2007) 62–129, http://dx.doi.org/10.1016/j.pmatsci.2006.06.001.

[23] I. Westermann, K.O. Pedersen, T. Furu, T. Børvik, O.S. Hopperstad, Effects of particles and solutes on strength, work-hardening and ductile fracture of aluminium alloys, Mech. Mater. 79 (2014) 58–72, http://dx.doi.org/10.1016/j.mechmat.2014.08.006.

[24] H. Tanihata, T. Sugawara, K. Matsuda, S. Ikeno, Effect of casting and homogenizing treatment conditions on the formation of Al-Fe-Si intermetallic compounds in 6063 Al-Mg-Si alloys, J. Mater. Sci. 34 (6) (1999) 1205–1210, http://dx.doi.org/10.1023/A:1004504805781.

[25] G. Mrówka-Nowotnik, J. Sieniawski, M. Wierzbiñska, Intermetallic phase particles in 6082 aluminium alloy, Arch. Mater. Sci. Eng. 28 (2) (2007) 69–76.

[26] S. Thomesen, O.S. Hopperstad, O.R. Myhr, T. Børvik, Influence of stress state on plastic flow and ductile fracture of three 6000-series aluminium alloys, Mater. Sci. Eng. A 783 (October 2019) (2020) 139295, http://dx.doi.org/10.1016/j.msea.2020.139295.

[27] G. Edwards, K. Stiller, G. Dunlop, M. Couper, The precipitation sequence in Al–Mg–Si alloys, Acta Mater. 46 (11) (1998) 3893–3904, http://dx.doi.org/10.1016/S1359-6454(98)00059-7, URL: https://linkinghub.elsevier.com/retrieve/pii/S1359645498000597.

[28] S.J. Andersen, H.W. Zandbergen, J. Jansen, C. Træholt, U. Tundal, O. Reiso, The crystal structure of the β'' phase in Al-Mg-Si alloys, Acta Mater. 46 (9) (1998) 3283–3298, http://dx.doi.org/10.1016/S1359-6454(97)00493-X.

[29] C.D. Marioara, S.J. Andersen, J. Jansen, H.W. Zandbergen, Atomic model for GP-zones in a 6082 Al-Mg-Si system, Acta Mater. 49 (2) (2001) 321–328, http://dx.doi.org/10.1016/S1359-6454(00)00302-5.

[30] G. Liu, J. Sun, C.-W. Nan, K.-H. Chen, Experiment and multiscale modeling of the coupled influence of constituents and precipitates on the ductile fracture of heat-treatable aluminum alloys, Acta Mater. 53 (12) (2005) 3459–3468, http://dx.doi.org/10.1016/j.actamat.2005.04.002, URL: https://linkinghub.elsevier.com/retrieve/pii/S1359645405002132.

[31] D.J. Lloyd, The scaling of the tensile ductile fracture strain with yield strength in Al alloys, Scr. Mater. 48 (2003) 341–344, http://dx.doi.org/10.1016/S1359-6462(02)00455-4.

[32] K.O. Pedersen, I. Westermann, T. Furu, T. Børvik, O.S. Hopperstad, Influence of microstructure on work-hardening and ductile fracture of aluminium alloys, Mater. Des. 70 (2015) 31–44, http://dx.doi.org/10.1016/j.matdes.2014.12.035.

[33] D. Dumont, A. Deschamps, Y. Brechet, On the relationship between microstructure, strength and toughness in AA7050 aluminum alloy, Mater. Sci. Eng. A 356 (1–2) (2003) 326–336, http://dx.doi.org/10.1016/S0921-5093(03)00145-X.

[34] G.G. Garrett, J.F. Knott, The influence of compositional and microstructural variations on the mechanism of static fracture in aluminum alloys, Metall. Trans. A 9 (9) (1978) 1187–1201, http://dx.doi.org/10.1007/BF02652242, URL: http://link.springer.com/10.1007/BF02652242.

[35] T. Pardoen, J.W. Hutchinson, Micromechanics-based model for trends in toughness of ductile metals, Acta Mater. 51 (1) (2003) 133–148, http://dx.doi.org/10.1016/S1359-6454(02)00386-5, URL: https://linkinghub.elsevier.com/retrieve/pii/S1359645402003865.

[36] R.O. Ritchie, The conflicts between strength and toughness, Nature Mater. 10 (11) (2011) 817–822, http://dx.doi.org/10.1038/nmat3115, URL: http://dx.doi.org/10.1038/nmat3115http://www.nature.com/articles/nmat3115.

[37] J.A. Walsh, K.V. Jata, E.A. Starke, Influence of Mn dispersoid content and stress state on ductile fracture of 2134 type Al alloys, Acta Metall. 37 (11) (1989) 2861–2871, http://dx.doi.org/10.1016/S0001-6160(89)80001-X.

[38] B. Dunwoody, D. Moore, A. Thomas, The effect of incoherent particles on toughness of an Al-Mg-Si alloy, J. Inst. Metals (1973) 172–175.

[39] J. Dowling, J. Martin, The influence of mn additions on the deformation behaviour of an Al-Mg-Si alloy, Acta Metall. 24 (1976) 1147–1153.

[40] K.C. Prince, J.W. Martin, The effects of dispersoids upon the micromechanisms of crack propagation in AlMgSi alloys, Acta Metall. 27 (8) (1979) 1401–1408, http://dx.doi.org/10.1016/0001-6160(79)90209-8.

[41] D. Broek, The role of inclusions in ductile fracture and fracture toughness, Eng. Fract. Mech. 5 (1) (1973) 55–66, http://dx.doi.org/10.1016/0013-7944(73)90007-6.

[42] T.B. Cox, J.R. Low Jr., An investigation of the plastic fracture of AISI 4340 and 18 Nickel-200 grade maraging steels, Metall. Trans. B 5 (6) (1974) 1457–1470, http://dx.doi.org/10.1007/BF02646633.

[43] M.A. Sutton, W. Zhao, M.L. Boone, A.P. Reynolds, D.S. Dawicke, Prediction of crack growth direction for mode I/II loading using small-scale yielding and void initiation/growth concepts, Int. J. Fract. 83 (3) (1997) 275–290, http://dx.doi.org/10.1023/A:1007339625267.

[44] R.H. Van Stone, T.B. Cox, J.R. Low, J.A. Psioda, Microstructural aspects of fracture by dimpled rupture, Int. Metals Rev. 30 (1) (1985) 157–180, http://dx.doi.org/10.1179/imtr.1985.30.1.157.

[45] F. Bron, J. Besson, A. Pineau, Ductile rupture in thin sheets of two grades of 2024 aluminum alloy, Mater. Sci. Eng. A 380 (1–2) (2004) 356–364, http://dx.doi.org/10.1016/j.msea.2004.04.008, URL: http://linkinghub.elsevier.com/retrieve/pii/S0921509304003806https://linkinghub.elsevier.com/retrieve/pii/S0921509304003806.

[46] V. Tvergaard, Ductile fracture by cavity nucleation between larger voids, J. Mech. Phys. Solids 30 (4) (1982) 265–286, http://dx.doi.org/10.1016/0022-5096(82)90033-3.

[47] D. Fabrègue, T. Pardoen, A constitutive model for elastoplastic solids containing primary and secondary voids, J. Mech. Phys. Solids 56 (3) (2008) 719–741, http://dx.doi.org/10.1016/j.jmps.2007.07.008.

[48] K.L. Nielsen, V. Tvergaard, Failure by void coalescence in metallic materials containing primary and secondary voids subject to intense shearing, Int. J. Solids Struct. 48 (9) (2011) 1255–1267, http://dx.doi.org/10.1016/j.ijsolstr.2011.01.008.

[49] V. Espeseth, D. Morin, J. Faleskog, T. Børvik, O.S. Hopperstad, A numerical study of a size-dependent finite-element based unit cell with primary and secondary voids, J. Mech. Phys. Solids 157 (June) (2021) 104493, http://dx.doi.org/10.1016/j.jmps.2021.104493.

[50] A.S. Argon, J. Im, Separation of second-phase particles in spheroidozied 1045 steel, Cu-0.6 straining, Metall. Trans. A 6 (1975) 839–851.

[51] Y. Shen, T.F. Morgeneyer, J. Garnier, L. Allais, L. Helfen, J. Crépin, Three-dimensional quantitative in situ study of crack initiation and propagation in AA6061 aluminum alloy sheets via synchrotron laminography and finite-element simulations, Acta Mater. 61 (7) (2013) 2571–2582, http://dx.doi.org/10.1016/j.actamat.2013.01.035.

[52] T. Petit, J. Besson, C. Ritter, K. Colas, L. Helfen, T.F. Morgeneyer, Effect of hardening on toughness captured by stress-based damage nucleation in 6061 aluminum alloy, Acta Mater. 180 (2019) 349–365, http://dx.doi.org/10.1016/j.actamat.2019.08.055.

[53] European Aluminium, Vision 2050, 2019, URL: https://www.european-aluminium.eu/media/2545/sample_vision-2050-low-carbon-strategy_20190401.pdf.

[54] S.K. Das, J.A. Green, Aluminum industry and climate change – assessment and responses, JOM 62 (2) (2010) 27–31.

[55] S.K. Das, J.A. Green, G. Kaufman, Aluminum recycling: Economic and environmental benefits, Light Metal Age 68 (1) (2010) 42–46.

[56] S.K. Das, W. Yin, X. Wen, Y. Liu, S. Ningileri, Formability evaluation of recycle-friendly automotive aluminum alloys, SAE Int. J. Mater. Manuf. 1 (1) (2008) 503–510, http://dx.doi.org/10.4271/2008-01-1095.

[57] A.J. Tomstad, S. Thomesen, T. Børvik, O.S. Hopperstad, Effects of constituent particle content on ductile fracture in isotropic and anisotropic 6000-series aluminium alloys, Mater. Sci. Eng. A 820 (April) (2021) http://dx.doi.org/10.1016/j.msea.2021.141420.

[58] K. Qvale, S. Thomesen, O.S. Hopperstad, T. Børvik, The effect of constituent particles on the tear resistance of three 6000-series aluminium alloys, Int. J. Fract. (2022) http://dx.doi.org/10.1007/s10704-022-00658-8, URL: https://doi.org/10.1007/s10704-022-00658-8https://link.springer.com/10.1007/s10704-022-00658-8.

[59] A.J. Tomstad, B.H. Frodal, T. Børvik, O.S. Hopperstad, Influence of particle content on the ductility of extruded non-recrystallized aluminium alloys subjected to shear loading, Mater. Sci. Eng. A (2022) 143409, http://dx.doi.org/10.1016/j.msea.2022.143409, URL: https://www.sciencedirect.com/science/article/pii/S0921509322008012.

[60] K. Marthinsen, J. Fridy, T. Rouns, K. Lippert, E. Nes, Characterization of 3-D particle distributions and effects on recrystallization kinetics and microstructure, Scr. Mater. 9 (39) (1998) 1177–1183.

[61] F. Hannard, A. Simar, E. Maire, T. Pardoen, Quantitative assessment of the impact of second phase particle arrangement on damage and fracture anisotropy, Acta Mater. 148 (2018) 456–466, http://dx.doi.org/10.1016/j.actamat.2018.02.003.

[62] J. Schindelin, I. Arganda-Carreras, E. Frise, V. Kaynig, M. Longair, T. Pietzsch, S. Preibisch, C. Rueden, S. Saalfeld, B. Schmid, J.Y. Tinevez, D.J. White, V. Hartenstein, K. Eliceiri, P. Tomancak, A. Cardona, Fiji: An open-source platform for biological-image analysis, Nature Methods 9 (7) (2012) 676–682, http://dx.doi.org/10.1038/nmeth.2019, arXiv:1081-8693.

[63] J. Ahrens, B. Geveci, C. Law, Paraview: An end-user tool for large data visualization, in: Visualization Handbook, 2005.

[64] E. Fagerholt, Ecorr 4.0, 2017, URL: https://folk.ntnu.no/egilf/ecorr/doc/, Last accessed 29 April 2022.

[65] G.T. Hahn, A.K. Mukherjee, A.R. Rosenfield, Plastic zone formation and stable crack growth in high-strength alloy sheets, Eng. Fract. Mech. 2 (3) (1971) 273–278, http://dx.doi.org/10.1016/0013-7944(71)90030-0.

[66] J.F. Knott, Fundamentals of Fracture Mechanics, Gruppo Italiano Frattura, 1973.

[67] H.G. Delorenzi, C.D. Shih, 3-D elastic-plastic investigation of fracture parameters in side-grooved compact specimen, Int. J. Fract. 21 (3) (1983) 195–220, http://dx.doi.org/10.1007/BF00963388.

[68] P. Poulose, Determination of fracture toughness from thin side-grooved specimens, Eng. Fract. Mech. 26 (2) (1987) 203–211, http://dx.doi.org/10.1016/0013-7944(87)90197-4, URL: https://linkinghub.elsevier.com/retrieve/pii/0013794487901974.

[69] Z. Fan, The grain size dependence of ductile fracture toughness of polycrystalline metals and alloys, Mater. Sci. Eng. Al 91 (1995) 73–83.

[70] T. Kobayashi, Strength and fracture of aluminum alloys, Mater. Sci. Eng. 286 (2000) URL: www.elsevier.com/locate/msea.

[71] J.R. Rice, The localization of plastic deformation, in: Proceedings of the 14th International Congress on Theoretical and Applied Mechanics, Vol. 1, 1976, pp. 207–220.

[72] A. Needleman, J. Rice, Limits to ductililty set by plastic flow localization, Mech. Sheet Metal Form. (1978) 237–265.

[73] H. Yamamoto, Conditions for shear localization in the ductile fracture of void-containing materials, Int. J. Fract. 14 (1978) 347–365, http://dx.doi.org/10.1007/BF00015989.

[74] D. Morin, O.S. Hopperstad, A. Benallal, On the description of ductile fracture in metals by the strain localization theory, Int. J. Fract. 209 (2018) 27–51, http://dx.doi.org/10.1007/s10704-017-0236-9, URL: http://link.springer.com/10.1007/s10704-017-0236-9.

[75] L.E.B. Dæhli, C. Tekoğlu, D. Morin, T. Børvik, O.S. Hopperstad, Ductile failure predictions using micromechanically-based computational models, J. Mech. Phys. Solids 164 (2022) 104873, http://dx.doi.org/10.1016/j.jmps.2022.104873.

[76] N.U. Deshpande, A.M. Gokhale, D.K. Denzer, J. Liu, Relationship between fracture toughness, fracture path, and microstructure of 7050 aluminum alloy: Part I. Quantitative characterization, Metall. Mater. Trans. A 29 (4) (1998) 1191–1201, http://dx.doi.org/10.1007/s11661-998-0246-3.

[77] P. Unwin, G. Smith, The microstructure and mechanical properties of Al-6 percent Zn-3 percent Mg, J. Inst. Metals 97 (10) (1969) 299–310.

[78] J.D. Embury, E. Nes, On the tensile fracture of aluminium alloys, Int. J. Mater. Res. 65 (1) (1974) 45–55.

[79] A.K. Vasudévan, R.D. Doherty, Grain boundary ductile fracture in precipitation hardened aluminium alloys, Acta Metall. 35 (6) (1987) 1193–1219, http://dx.doi.org/10.1016/0001-6160(87)90001-0.

[80] M. Nakai, T. Eto, New aspect of development of high strength aluminum alloys for aerospace applications, Mater. Sci. Eng. A 285 (1–2) (2000) 62–68, http://dx.doi.org/10.1016/S0921-5093(00)00667-5, URL: https://dl.acm.org/doi/10.1145/240806.240810https://linkinghub.elsevier.com/retrieve/pii/S0921509300006675.

[81] R.J. Bourcier, D.A. Koss, R.E. Smelser, O. Richmond, The influence of porosity on the deformation and fracture of alloys, Acta Metall. 34 (12) (1986) 2443–2453, http://dx.doi.org/10.1016/0001-6160(86)90147-1.

[82] A. Weck, D.S. Wilkinson, E. Maire, Observation of void nucleation, growth and coalescence in a model metal matrix composite using X-ray tomography, Mater. Sci. Eng. A 488 (1–2) (2008) 435–445, http://dx.doi.org/10.1016/j.msea.2007.11.050.

[83] N. Pathak, J. Adrien, C. Butcher, E. Maire, M. Worswick, Experimental stress state-dependent void nucleation behavior for advanced high strength steels, Int. J. Mech. Sci. 179 (March) (2020) 105661, http://dx.doi.org/10.1016/j.ijmecsci.2020.105661.

[84] M.M. Arani, N.S. Ramesh, X. Wang, N. Parson, M. Li, W.J. Poole, The localization of plastic deformation in the precipitate free zone of an Al-Mg-Si-Mn alloy, Acta Mater. 231 (2022) http://dx.doi.org/10.1016/j.actamat.2022.117872.

[85] O.R. Myhr, T. Børvik, C.D. Marioara, S. Wenner, O.S. Hopperstad, Nanoscale modelling of combined isotropic and kinematic hardening of 6000 series aluminium alloys, Mech. Mater. 151 (2020) http://dx.doi.org/10.1016/j.mechmat.2020.103603.

[86] M. Khadyko, C.D. Marioara, I.G. Ringdalen, S. Dumoulin, O.S. Hopperstad, Deformation and strain localization in polycrystals with plastically heterogeneous grains, Int. J. Plast. 86 (2016) 128–150, http://dx.doi.org/10.1016/j.ijplas.2016.08.005.

[87] T. Pardoen, D. Dumont, a. Deschamps, Y. Brechet, Grain boundary versus transgranular ductile failure, J. Mech. Phys. Solids 51 (4) (2003) 637–665, http://dx.doi.org/10.1016/S0022-5096(02)00102-3.